

Setting the stage for the search for life with the Habitable Worlds Observatory: Properties of 164 promising planet survey targets

CALEB K. HARADA ^{1,*}, COURTNEY D. DRESSING ¹, STEPHEN R. KANE ², AND BAHAREH ADAMI ARDESTANI^{3,1}

¹*Department of Astronomy, 501 Campbell Hall #3411, University of California, Berkeley, CA 94720, USA*

²*Department of Earth and Planetary Sciences, University of California, Riverside, CA 92521, USA*

³*Sonoma State University, Rohnert Park, CA 94928, USA*

(Received January 5, 2024; Revised February 29, 2024; Accepted March 1, 2024)

Submitted to AAS Journals

ABSTRACT

The Decadal Survey on Astronomy and Astrophysics 2020 (Astro2020) has recommended that NASA realize a large IR/O/UV space telescope optimized for high-contrast imaging and spectroscopy of ~ 25 exo-Earths and transformative general astrophysics. The NASA Exoplanet Exploration Program (ExEP) has subsequently released a list of 164 nearby ($d < 25$ pc) targets deemed the most accessible to survey for potentially habitable exoplanets with the Habitable Worlds Observatory (HWO). We present a catalog of system properties for the 164 ExEP targets, including 1744 abundance measurements for 14 elements from the Hypatia Catalog and 924 photometry measurements spanning from 151.6 nm to 22 μm in the *GALEX*, Strömgren, Tycho, *Gaia*, 2MASS, and *WISE* bandpasses. We independently derive stellar properties for these systems by modeling their spectral energy distributions with Bayesian model averaging. Additionally, by consulting the literature, we identify *TESS* flare rates for 46 stars, optical variability for 78 stars, and X-ray emission for 46 stars in our sample. We discuss our catalog in the context of planet habitability and draw attention to key gaps in our knowledge where precursor science can help to inform HWO mission design trade studies in the near future. Notably, only 33 of the 164 stars in our sample have reliable space-based UV measurements, and only 40 have a mid-IR measurement. We also find that phosphorus, a bio-essential element, has only been measured in 11 of these stars, motivating future abundance surveys. Our catalog is publicly available and we advocate for its use in future studies of promising HWO targets.

Keywords: Exoplanet catalogs (488), Exoplanet astronomy (486), Planet hosting stars (1242), Astrobiology (74), Space telescopes (1547)

1. INTRODUCTION

The Astro2020 Decadal Survey has recommended that NASA devise a large (~ 6 m inscribed diameter), stable, space-based infrared/optical/ultraviolet (IR/O/UV) telescope capable of high-contrast (10^{-10}) imaging and spectroscopy (National Academies of Sciences, Engineering, and Medicine 2021). Currently named the Habitable Worlds Observatory (HWO) and

targeted to launch in the 2040s, the mission's primary science goals will be to search for biosignatures roughly 25 habitable zone (HZ) exoplanets, while simultaneously enabling transformative general astrophysics (National Academies of Sciences, Engineering, and Medicine 2021).

The Astro2020 report recognized that the unprecedented nature of HWO's science objectives and technology requirements will require sophisticated planning and review leading up to the mission design stage. Astro2020 therefore recommended a Great Observatory Mission and Technology Maturation Program (GOMAP) whose aim is to make early significant investments in the co-

Corresponding author: Caleb K. Harada
charada@berkeley.edu

* NSF Graduate Research Fellow

maturation of mission concepts and technologies prior to ultimate recommendation and implementation (National Academies of Sciences, Engineering, and Medicine 2021). The outcomes of the GOMAP phase will inform the final design of HWO.

Following the release of Astro2020, the NASA Exoplanet Exploration Program (ExEP) created a Mission Star List¹ for HWO that included 164 stars “whose [hypothetical] exo-Earths would be the most accessible for a systematic imaging survey of habitable zones with a 6-m class space telescope in terms of angular separation, planet brightness in reflected light, and planet-star brightness ratio” (Mamajek & Stapelfeldt 2023). The ExEP Mission Star List (EMSL) was compiled by analyzing nearby bright stars and adopting inputs from the the mission studies for the Large UV/Optical/IR Surveyor (LUVOIR; The LUVOIR Team 2019) and the Habitable Exoplanet Observatory (HabEx; Gaudi et al. 2020). The broad scope of the list was intended to avoid being overly prescriptive in the required starlight suppression technology or mission requirements (Mamajek & Stapelfeldt 2023).

However, while the EMSL contained key observability metrics that were calculated to constrain the sample (e.g., angular separation, contrast ratio between the planet and host star, excess levels of complicating exozodiacal dust, etc.), it lacked other information that may be crucial for identifying a robust sample of potential exo-Earths. For example, the high-energy spectrum of the host star can significantly impact habitability (e.g., Segura et al. 2003; Rugheimer et al. 2015b; Roettenbacher & Kane 2017), but the EMSL does not include UV or X-ray radiation measurements. Host star composition, which reflects the composition of the protoplanetary disk, is linked to the outcomes of planet formation and hence may give us hints as to which targets are more or less likely to host habitable rocky planets (e.g., Gáspár et al. 2016; Santos et al. 2017; Adibekyan et al. 2021; Cabral et al. 2023). While the EMSL includes the host star metallicity [Fe/H], it is known that the iron abundance alone does not provide a robust proxy for scaling the abundances of other planet-building elements (e.g., Bitsch & Battistini 2020; Jorge et al. 2022).

Starting with the EMSL targets², in this work we construct a catalog of properties of promising nearby targets for the HWO exo-Earth survey. As a step toward building a more complete understanding of these systems and their likelihood of hosting exo-Earths, our cat-

alog contains key properties of these stars that are theorized to be linked to planet habitability. This work, and subsequent precursor science studies, will reduce HWO mission design risk by enabling science and engineering trades that will weigh how key design choices and astrophysical realities may impact the yield of potentially habitable planets characterized by HWO. For example, identifying and characterizing the most promising HWO targets early in mission development will inform critical mission requirements such as inner working angle (IWA), outer working angle (OWA), field of regard, sensitivity, settling time, slew speed, wavelength coverage, and number of filters used for detection and characterization of potentially habitable planets. This work is complementary to the Habitable Worlds Observatory Preliminary Input Catalog (HPIC; Tuchow et al. 2024), which became public during the revision process of this paper.

The rest of this paper is organized as follows. In Section 2, we describe the information we have compiled in this catalog, which includes the original EMSL data, photometry from 6 different surveys, 14 elemental abundances, flare rates, stellar variability, and X-ray detections. In Section 3, we describe our analysis of stellar properties derived from SED fitting and the verification of stellar abundances from the literature. We discuss our results and implications of our catalog in Section 4, and conclude in Section 5.

2. DATA

2.1. The ExEP Mission Star List

Motivated by the Astro2020 Decadal Survey, Mamajek & Stapelfeldt (2023) created the ExEP Mission Star List (EMSL) with 164 bright stars whose exo-Earths would be the most accessible for a systematic imaging survey of nearby HZs. To allow flexibility in HWO mission design trade studies and the mission target list, they considered different constraints on the observatory’s IWA, exoplanet brightness limits, planet-to-star brightness ratio, the presence of circumstellar debris disks, and stellar multiplicity. Their sample was limited to nearby stars whose HZs would be accessible to a 6-meter-class telescope with starlight suppression technology (capable of contrast down to 2.5×10^{-11} in R_c band), and whose HZ terrestrial planets would be bright enough to image and spectroscopically characterize on relatively short timescales (planet magnitudes of $R_c \leq 31$ for integration times up to 60 days; Mamajek & Stapelfeldt 2023). We briefly summarize their results in this section.

Following the LUVOIR and HabEx mission studies (The LUVOIR Team 2019; Gaudi et al. 2020), Mamajek & Stapelfeldt (2023) assumed an occurrence rate of ter-

¹ https://exoplanetarchive.ipac.caltech.edu/docs/2645_NASA_ExEP_Target_List_HWO_Documentation_2023.pdf

² We will consider a broader set of stars in future work.

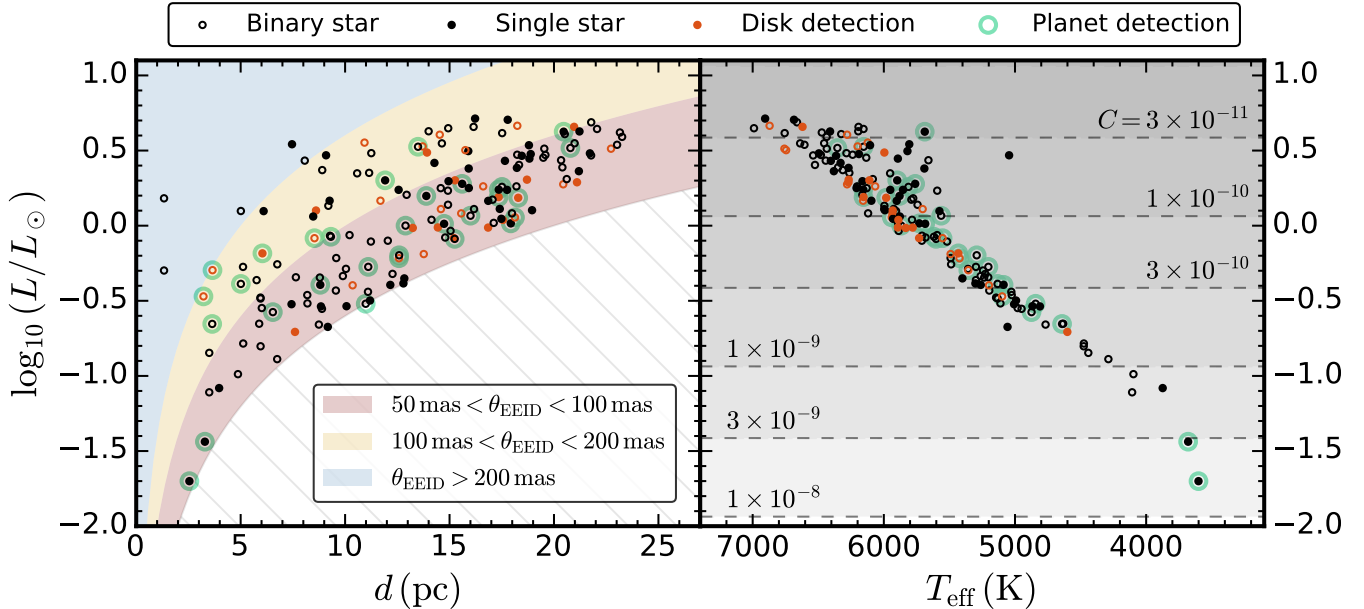


Figure 1. *Left:* EMSL stellar luminosity vs. distance (data from Mamajek & Stapelfeldt 2023). The shaded areas show different ranges of the Earth-Equivalent Instellation Distance (EEID) in angular units. *Right:* H-R Diagram for EMSL stars. The shaded intervals show the expected planet-to-star contrast ratio for a $1 R_{\oplus}$ planet at the EEID, assuming a geometric albedo of $p = 0.2$ at a phase angle of $\alpha = 90^{\circ}$. In both panels, the closed circles show single stars, while the open circles show stars in binary systems with angular separations $> 3''$. The red circles indicate the presence of a circumstellar debris disk, and the green rings highlight systems known to host at least one planet.

restrial HZ planets of $\eta_{\oplus} = 0.24$, thus requiring a sample of at least ~ 100 targets to achieve the Astro2020 goal of imaging 25 exo-Earths. Their calculations adopted the conservative habitable zone limits, defined as the range of semi-major axes between 0.95-1.67 au for a solar twin for planets between 0.8 - $1.4 R_{\oplus}$ (e.g., Kasting et al. 1993; Kopparapu et al. 2013). For other stars, they scaled the semi-major axis limits by the square root of the solar-normalized stellar luminosity.

Starting from a large initial sample of nearby AFGKM stars, which was descended from the Extreme Precision Radial Velocity (EPRV) Working Group Final Report³ (Crass et al. 2021), the EMSL was constructed by filling in additional targets from various sources with overlapping spectral types, magnitudes, and distances. For this volume-limited sample of approximately 800 stars, Mamajek & Stapelfeldt (2023) calculated the angular separation and expected planet brightness assuming 12 different scenarios with various combinations of orbital distance, phase angle, and planet radius.

In their calculations, Mamajek & Stapelfeldt (2023) adopted Cousins R_c band photometry because of the R_c

filter’s overlapping wavelength coverage with the LUV-IOR and HabEx bandpasses. Following the LUVOR and HabEx mission studies, they assumed a planetary geometric albedo of $p = 0.2$ for all systems. Then, for each star, they calculated the Earth-equivalent instellation distance (EEID), defined as the orbital separation at which a planet receives the equivalent flux as Earth at 1 au:

$$r_{\text{EEID}} = 1 \text{ au} \sqrt{L_{\star}/L_{\odot}} \quad (1)$$

where L_{\star} is the stellar luminosity⁴. Assuming a circular orbit and maximum angular separation, this can also be written in terms of the projected angular separation (in milliarcseconds) as $\theta_{\text{EEID}} = r_{\text{EEID}}/d_{\text{pc}} = r_{\text{EEID}}\varpi_{\text{mas}}$, where d_{pc} is the distance to the star in parsecs and ϖ_{mas} is the parallax angle in milliarcseconds.

Mamajek & Stapelfeldt (2023) then calculated the planet-to-star brightness ratio (i.e., contrast) as

$$C = F_p/F_{\star} = p\phi(\alpha)(R_p/r)^2 \quad (2)$$

where p is the geometric albedo, $\phi(\alpha)$ is the integral phase function at phase angle α (i.e., the observer-planet-star angle), R_p is the planet’s radius, and r is the

³ The EPRV Working Group target list was itself drawn from the LUVOR and HabEx study reports (The LUVOR Team 2019; Gaudi et al. 2020).

⁴ Note that this basic scaling relation does not account for the detailed spectra of non-solar type stars, which can influence the actual amount of flux received by a planet and hence its temperature.

Table 1. Summary of EMSL tier criteria (reproduced from Mamajek & Stapelfeldt 2023).

Parameter	Tier A	Tier B	Tier C
Number of stars	47	51	66
IWA constraint	83 mas	72 mas	65 mas
Planet brightness limit (R_c)	30.5	31.0	31.0
Planet-to-star contrast limit	4×10^{-11}	4×10^{-11}	2.5×10^{-11}
Disk criterion	No known dust disks of any kind.	No disk; or Kuiper Belt disk permitted if $L_{\text{disk}}/L_{\star} \leq 10^{-4}$.	All disks permitted.
Treatment of binaries	Single or binary companion at $> 10''$ sep.	Single or binary companion at $5 - 10''$ sep.	Single or binary companion at $3 - 5''$ sep.

separation between the planet and its host star. They assumed that all planets had circular orbits (such that r is equivalent to the semi-major axis a) and adopted a simple Lambertian phase function for isotropic scattering:

$$\phi(\alpha) = \frac{1}{\pi} [\sin \alpha + (\pi - \alpha) \cos \alpha]. \quad (3)$$

The hypothetical planet’s R_c magnitude was then calculated from the contrast ratio as

$$R_{c,p} = R_{c,\star} - 2.5 \log_{10} C \quad (4)$$

where $R_{c,\star}$ is the magnitude of the host star.

The initial ~ 800 systems were ranked by the number of test scenarios (out of 12) where the hypothetical planet satisfied pre-defined limits on angular separation, contrast ratio, and apparent planet R_c magnitude. These limits were informed by the predicted performance of future direct-imaging technology currently under development for HWO (Mamajek & Stapelfeldt 2023). Further constraints on the presence of debris disks and stellar multiplicity narrowed down the final EMSL list to 164 targets, which were then assigned to a tier (A, B, or C). The authors considered tier A to be the “best” targets for an HWO exo-Earth survey, while tiers B and C contained targets with one or more issues which made them less optimal than tier A. The final

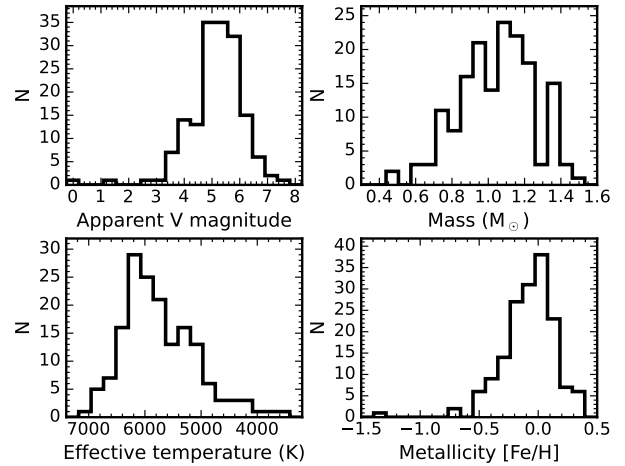


Figure 2. Histograms of the apparent V magnitudes, stellar masses, effective temperatures, and metallicities of EMSL stars (data from Mamajek & Stapelfeldt 2023).

EMSL contained 47 stars in tier A, 61 in tier B, and 66 in tier C. The criteria defined by Mamajek & Stapelfeldt (2023) for each tier are summarized in Table 1, and we refer the reader to the original ExEP report for more detailed discussion of the selection criteria.

We accessed the most up-to-date version of the EMSL⁵ via the NASA Exoplanet Archive Table Access Protocol (TAP). In this work, we include each of the EMSL table columns as they were originally reported, with some minor corrections. Appendix A lists minor inconsistencies that we identified and subsequently corrected in our catalog (e.g., the EMSL table that we downloaded contained an empty column that we remove in our catalog).

We plot the full sample of EMSL stars in the luminosity-distance plane and in the H-R diagram in Figure 1. Figure 2 shows histograms of the apparent V magnitude, stellar mass, effective temperature, and metallicity of the EMSL sample. Figure 3 demonstrates the range of angular separations and magnitude differences between binary stars across the sample. All values plotted in Figures 1, 2, and 3 are taken from the original EMSL (Mamajek & Stapelfeldt 2023).

In the following sections, we expand upon the original EMSL by adding columns with additional system properties. A summary of all column names, descriptions, units, and references in our catalog (and the EMSL) are provided in Table 4 in Appendix B.

2.2. Photometry

⁵ https://exoplanetarchive.ipac.caltech.edu/cgi-bin/TblView/nph-tblView?app=ExoTbls&config=DLSTARS_EXEP

For each of the 164 EMSL stars we searched for archival photometry spanning 151.6 nm to 22 μm . In order to accurately crossmatch the sources in the EMSL table with various photometric catalogs, we first crossmatched the EMSL stars with the *TESS* Input Catalog⁶ (TIC; Stassun et al. 2019) using the TIC ID provided in the EMSL. From the TIC, we obtained *Gaia* DR2 IDs, which were then crossmatched to *Gaia* DR3 IDs using the *Gaia* DR3 `dr2_neighbourhood` crossmatch table⁷ (Gaia Collaboration et al. 2023). For sources without a *Gaia* DR2 ID, we used the *HIPPARCOS* ID provided in the EMSL to crossmatch the sources with *Gaia* DR3. We identified *Gaia* DR3 IDs for all sources except for α Cen A, which is the brightest star in our sample ($V \sim 0$) and too bright for *Gaia*.

2.2.1. *Gaia* DR3

Using the crossmatched *Gaia* DR3 IDs, we obtained *Gaia* optical photometry and associated uncertainties in the G (330 – 1050 nm), G_{BP} (330 – 680 nm), and G_{RP} (630 – 1050 nm) bandpasses from the *Gaia* DR3 `gaia_source` table⁸ (Gaia Collaboration et al. 2016, 2023), which we accessed via VizieR⁹. Due to quality issues that we attribute to detector saturation, we do not include *Gaia* photometry for α Cen A/B.

2.2.2. *AllWISE*

We obtained mid-infrared photometry from the Wide-field Infrared Survey Explorer (*WISE*; Wright et al. 2010) in four bandpasses: W_1 (3.4 μm), W_2 (4.6 μm), W_3 (12 μm), and W_4 (22 μm). Using the *Gaia* DR3 `allwise_best_neighbour` table¹⁰ (Gaia Collaboration et al. 2023), we crossmatched the *Gaia* DR3 IDs of our target stars to their respective identifiers in the AllWISE Catalog (Cutri et al. 2021), which we accessed using VizieR, and collected the photometry and associated uncertainties for each source where it was available. We do not include any photometry reported to be blended with extended sources, or otherwise flagged as contaminated or poor quality ($\text{SNR} < 2$). We find measurements satisfying these criteria for 17, 19, 33, and 40 stars in the W_1 , W_2 , W_3 , and W_4 bandpasses, respectively.

2.2.3. *2MASS*

⁶ Accessed from the Mikulski Archive for Space Telescopes (MAST) via `astroquery` (Astropy Collaboration et al. 2013, 2018).

⁷ https://gaia.aip.de/metadata/gaiaedr3/dr2_neighbourhood/

⁸ https://gaia.aip.de/metadata/gaiaedr3/gaia_source/

⁹ <https://vizier.cds.unistra.fr/viz-bin/VizieR>

¹⁰ https://gaia.aip.de/metadata/gaiaedr3/allwise_best_neighbour/

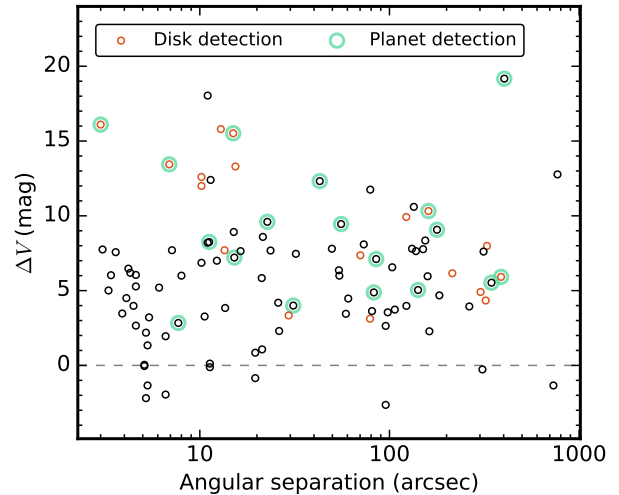


Figure 3. Angular separation vs. difference in apparent V magnitude for EMSL binary star systems (data from Mamajek & Stapelfeldt 2023). As in Figure 1, the red circles show systems with a debris disk, and the green rings indicate systems with at least one known planet.

We followed a similar procedure to acquire near-infrared photometry. We used the *Gaia* DR3 `tmass_psc_xsc_best_neighbour` table¹¹ (Gaia Collaboration et al. 2023) to crossmatch the *Gaia* DR3 IDs of our target stars to their respective The Two Micron All Sky Survey (2MASS; Skrutskie et al. 2006) identifiers. We then used the 2MASS IDs to obtain J (1.24 μm), H (1.66 μm), and K_s (2.16 μm) photometry and associated uncertainties from the 2MASS All-Sky Catalog of Point Sources (Cutri et al. 2003) on VizieR. We excluded any data with an extended source contamination flag or artifact contamination and confusion flag. We also removed any bad photometry indicated by a photometric quality flag of “X,” “U,” “F,” or “E.” This resulted in J band photometry for 130 stars, H band photometry for 127 stars, and K_s band photometry for 95 stars.

2.2.4. *Tycho-2*

In the optical, we added space-based photometry from the Tycho-2 Catalogue of the 2.5 Million Brightest Stars (Høg et al. 2000), with measurements from the ESA *HIPPARCOS* satellite’s Star Mapper. We crossmatched the *Gaia* DR3 IDs of our stars to their Tycho-2 identifiers using the *Gaia* DR3 `tycho2tdsc_merge_best_neighbour` table¹² (Gaia Collaboration et al. 2023), then obtained B_T (430 nm) and

¹¹ https://gaia.aip.de/metadata/gaiaedr3/tmass_psc_xsc_best_neighbour/

¹² https://gaia.aip.de/metadata/gaiaedr3/tycho2tdsc_merge_best_neighbour/

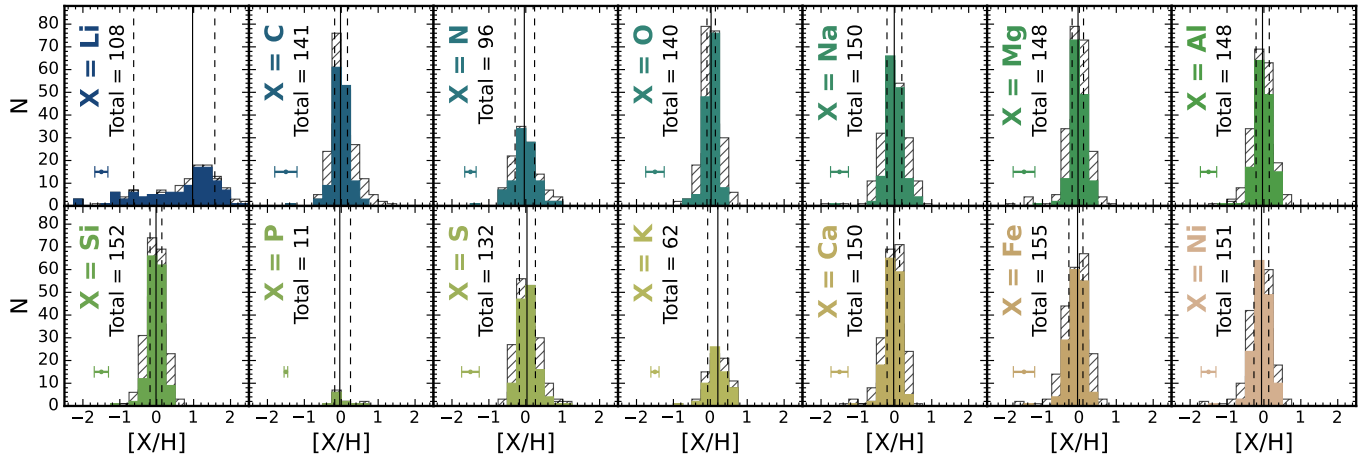


Figure 4. Histograms of the 14 stellar abundances retrieved from the Hypatia Catalog (Hinkel et al. 2014). For stars with multiple measurements of the same element, the shaded histograms are computed assuming the mean abundance value and the gray hatched histograms are computed assuming the minimum and maximum abundance values. The element name and corresponding number of stars with at least one abundance measurement for that element are labeled in each panel, and a representative errorbar showing the average difference between the minimum and maximum abundance values is shown in the lower left-hand corner. The vertical lines show the sample median values, and the dashed lines show the 16th and 84th percentiles. Note that the lithium abundances show the greatest amount of spread across the sample due to the strong dependence of $[\text{Li}/\text{H}]$ on stellar age.

V_T (530 nm) photometry and associated uncertainties from the Tycho-2 Catalog on VizieR using the cross-matched IDs. We found both B_T and V_T photometry for a total of 132 stars in our sample.

2.2.5. Strömgren

We obtained additional ground-based UV/optical photometry from the Strömgren-Crawford $uvby\beta$ Photometry Catalog (Paunzen 2015) on VizieR. We cross-matched our sources with the Paunzen (2015) Catalog using their Tycho-2 IDs identified in the previous section. We collected photometry and associated uncertainties in the Strömgren u (350 nm), v (411 nm), b (467 nm), and y (547 nm) bandpasses for 130 of our catalog stars.

2.2.6. GALEX

Finally, we obtained UV photometry from the Galaxy Evolution Explorer (*GALEX*; Martin et al. 2005), which includes two bands at 135-175 nm (FUV) and 175-275 nm (NUV). We used the `astroquery` Xmatch service (Astropy Collaboration et al. 2013, 2018) to cross-match the *Gaia* DR3 coordinates of our target stars with any *GALEX* sources within a $30''$ radius in the Revised Catalog of *GALEX* Ultraviolet Sources (Bianchi et al. 2017). We collected the FUV and NUV magnitudes with their respective uncertainties of the nearest neighbor *GALEX* source, and excluded any measurements whose associated artifact or extraction flags were > 0 . We report reliable *GALEX* measurements for 27 stars in the FUV and 12 stars in the NUV.

2.3. Stellar abundances

The Hypatia Catalog is a publicly available spectroscopic abundance catalog consisting of data from 84 literature sources for 50 elements across 3058 stars within 150 pc of the Sun (Hinkel et al. 2014). We obtained stellar abundances for 14 elements from the Hypatia Catalog, including key terrestrial planet building blocks (e.g., Si, Mg, Al, Fe, and Ni) as well as elements that are essential for life on Earth (e.g., C, N, O, P, and S). All of the retrieved abundances were normalized assuming solar values from Asplund et al. (2009).

We queried the catalog using the Hypatia API¹³, first attempting to crossmatch sources with the Tycho-2 IDs. If the Tycho-2 ID initially failed to return a match, we iteratively reattempted the query using the 2MASS ID, HD name, common name, and finally the *Gaia* DR2/DR3 ID. For each successful match, we collected all available abundance measurements for the elements listed in Table 2, and recorded the mean, minimum, maximum, and standard deviation of the reported values. In cases where only a single abundance measurement was reported for a given element, we assigned an uncertainty equivalent to the median abundance uncertainty of all the other stars in the sample. For completeness, we also include the total number of abundance values per element for each star in our catalog, in addition

¹³ <https://www.hypatiacatalog.com/api>

to the original literature references for the minimum and maximum abundance values.

A summary of the retrieved abundances is provided in Table 2. Histograms of the mean, minimum, and maximum abundance values are shown in Figure 4.

2.4. Stellar flare rates

We include estimated flare rates for our sample based on light curve observations from the Transiting Exoplanet Survey Satellite (*TESS*) Mission Ricker et al. (2014). Using data from the first 39 sectors of *TESS* observations, Pietras et al. (2022) presented a statistical analysis and extensive catalog of stellar flare events identified in the 2-minute cadence light curves of 330,000 stars using an automated detection pipeline called WARPFINDER. We used the TIC identifiers of our targets to crossmatch our catalog with the flare events reported in the Pietras et al. (2022) flare catalog.

For each crossmatched source, we recorded the number of flares detected (in the first 39 sectors of *TESS* observations), in addition to the relative amplitude and estimated total energy released by the most energetic flare. Then, using the `lightkurve` package (Lightkurve Collaboration et al. 2018) to access all two-minute cadence *TESS* observations of each target on MAST, we determined the number of *TESS* sectors with observations and how many of these sectors were observed up to sector 39. We note that 148 of our stars have at least one sector of *TESS* observations, and the median number of *TESS* sectors observed per star is 3. Using this information, combined with the known duration of each sector (27.4 days; Ricker et al. 2014), we calculated the stellar flare rate (in s^{-1}) for each star with at least one flare detected by Pietras et al. (2022). We identified 44 such stars in our sample.

For completeness, we also checked for flares using the Yang et al. (2023) catalog of stellar flares from *TESS*. Using data from cycles 1-30 of *TESS*, Yang et al. (2023) independently measured 60,810 flare events from 13,478 stars. We identified two additional flare sources in the Yang et al. (2023) catalog that were not found in the Pietras et al. (2022) sample of 44 stars: HD 166 and GJ 811. For these two targets, we recorded the number of flares detected in the first 30 sectors of *TESS* observations and the relative amplitude and energy released by the most energetic flare (Yang et al. 2023). We also estimated the flare rate following the procedure described above. A histogram of all 46 *TESS* flare rates and a plot of the flare energy as a function of stellar effective temperature are shown in Figure 5.

Lastly, we also searched the literature for stellar flare information at higher-energy wavelengths. We identi-

Table 2. Summary of stellar abundances retrieved from the Hypatia catalog (Hinkel et al. 2014).

Element	# Stars	# Meas.	Min. (dex)	Median (dex)	Max. (dex)
[Li/H]	108	361	-2.11	0.97	2.37
[C/H]	141	803	-1.27	-0.02	0.66
[N/H]	96	165	-1.41	-0.04	0.76
[O/H]	140	928	-0.71	0.02	0.38
[Na/H]	150	1200	-1.58	-0.02	0.56
[Mg/H]	148	1143	-1.13	-0.04	0.42
[Al/H]	148	1030	-1.22	-0.04	0.49
[Si/H]	152	1438	-1.1	-0.02	0.43
[P/H]	11	17	-0.28	-0.04	0.54
[S/H]	132	504	-0.46	0.03	1.02
[K/H]	62	88	-0.81	0.2	0.62
[Ca/H]	150	1192	-1.09	-0.03	0.36
[Fe/H]	155	2811	-1.3	-0.05	0.39
[Ni/H]	151	1381	-1.38	-0.06	0.46

fied 7 systems in our catalog with X-ray flare detections. These X-ray flares were identified in the XMM-Newton serendipitous source catalogue (Pye et al. 2015) for 61 Cyg A/B, 70 Oph A/B, ξ Boo A, HD 95735, 3 UMa, ϵ Eri, and κ 1 Cet. In our catalog, we include an X-ray flare detection flag for these sources.

2.5. Stellar variability

We obtained stellar variability information for our stars using the Variability Catalog of Stars Observed during the *TESS* Prime Mission (Fetherolf et al. 2023). This catalog contains over 84,000 periodic variables (with periods ranging from 0.01-13 days) identified with high or moderate confidence, including \sim 65,000 variable stars that were not previously identified in the literature (Fetherolf et al. 2023).

We used the TIC identifiers to crossmatch our targets with the Fetherolf et al. (2023) variability catalog, which we downloaded from the MAST. For each crossmatched source, we collected the type of variability solution (i.e., single or double sinusoid or autocorrelation function; Fetherolf et al. 2023) in addition to the variability period(s) and amplitude(s). The single sinusoid periodic signals can indicate a variety of stellar activity, including rotational variations caused by starspot activity, a dominant pulsation mode, or ellipsoidal variations in stellar binaries (Fetherolf et al. 2023). On the other hand, double sinusoid solutions are preferred for stars with multiple dominant periodic-

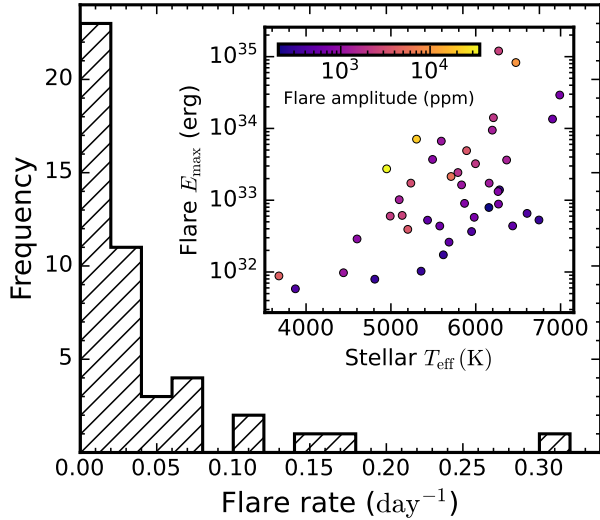


Figure 5. Histogram of stellar flare rates from *TESS*, calculated using the results of Pietras et al. (2022) and Yang et al. (2023). The inset plot shows the estimated energy released by the most energetic flare as a function of stellar effective temperature. The colorbar indicates the measured relative flare amplitude.

ities, such as multimodal pulsations or differential stellar rotation, while autocorrelation function (ACF) solutions typically represent short-period eclipsing binary systems or periodic non-sinusoidal rotational variability (Fetherolf et al. 2023).

We found 78 stars in our sample with an indication of variability in the *TESS* photometry. Figure 6 shows examples of *TESS* light curves, which we downloaded from the MAST using the *Lightkurve* package (Lightkurve Collaboration et al. 2018), for stars with different variability solutions identified by Fetherolf et al. (2023). We plot the luminosity of these stars as a function of their variability period in Figure 7.

For completeness, and to search for variable sources with periods longer than 13 days, we also queried the American Association of Variable Star Observers (AAVSO) International Variable Star Index (VSX). This comprehensive variability catalog combines variable star observations from multiple published sources utilizing both ground- and space-based photometry¹⁴. We successfully crossmatched 65 of our stars with the VSX catalog classified as either “variable” or “suspected variable,” of which 30 were not included in the Fetherolf et al. (2023) *TESS* catalog. For each of these 65 stars, we provide a URL link to the respective VSX entry in our catalog.

¹⁴ <https://www.aavso.org/vsx/index.php?view=about.top>

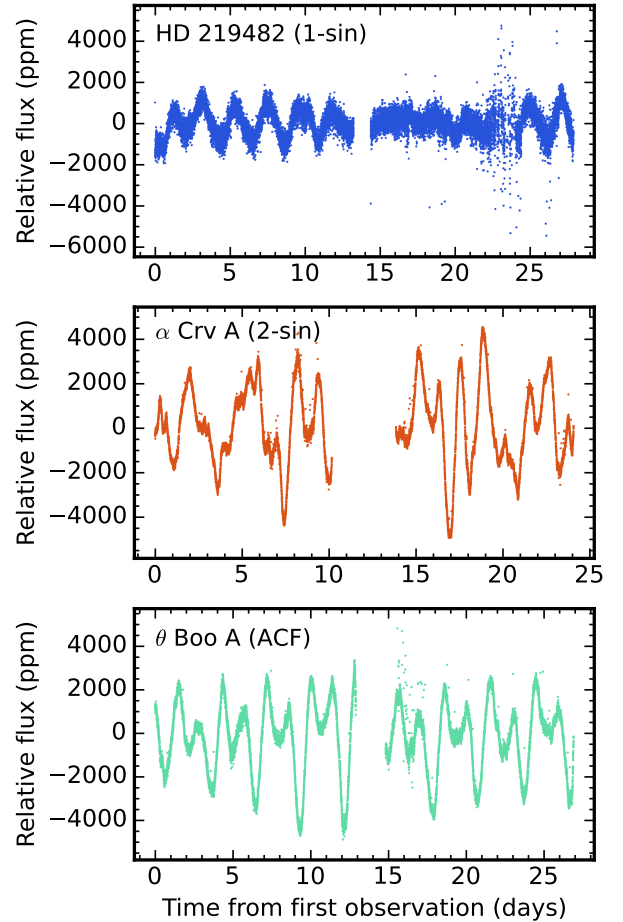


Figure 6. Example *TESS* light curves for variable stars in our sample identified by Fetherolf et al. (2023). The top panel shows an example of a single sinusoid solution for HD 219482, the middle panel shows a double sinusoid solution for α Crv A, and the bottom panel shows an ACF solution for θ Boo A. The data used to create this figure were downloaded from MAST using the *Lightkurve* package (Lightkurve Collaboration et al. 2018).

2.6. X-ray emission

Finally, we identified sources in our catalog with previous X-ray detections by crossmatching our sample with the Millions of Optical-Radio/X-ray Associations (MORX) Catalogue (Flesch 2016, 2023). MORX combines published optical, radio, and X-ray sky catalogs to match probable radio/X-ray associations with optical counterparts for over 3 million sources. The catalog includes X-ray detections from the *Chandra* (Weisskopf et al. 2000), *XMM-Newton* (Jansen et al. 2001), *Swift* (Burrows et al. 2005), and *ROSAT* (Voges et al. 1999) satellite missions.

We used VizieR and the *astroquery* Xmatch service (Astropy Collaboration et al. 2013, 2018) to cross-match the *Gaia* DR3 coordinates of our targets with

any sources identified in the MORX catalog within a $30''$ radius. We collected the *Chandra*, *XMM-Newton*, *Swift*, and/or other identifiers of the best neighbor X-ray source. We verified that each crossmatched source was classified as a star and an X-ray source by checking the corresponding quality flags and requiring that the MORX algorithm was $> 80\%$ confident in its classification. We identified 41 of our targets in the MORX catalog, bringing the total number of sources in our catalog with X-ray emission up to 46 (including the X-ray flare detections described in Section 2.4).

3. ANALYSIS

3.1. Stellar SED fitting

Using the photometry collected from the literature (described in Section 2.2), we constructed spectral energy distributions (SEDs) for each star in our catalog. We then used the open source ARIADNE package (Vines & Jenkins 2022) to fit synthetic SED models to the data in order to independently constrain stellar radii (R_*), masses (M_*), effective temperatures (T_{eff}), and luminosities (L_*).

ARIADNE leverages Bayesian Model Averaging (BMA; e.g., Fragoso et al. 2018) and nested sampling techniques (e.g., Skilling 2004, 2006) to accurately predict stellar properties from SEDs. The advantage of BMA is that it addresses systematic biases between different stellar atmosphere models by incorporating information from each one to arrive at a solution. Specifically, ARIADNE incorporates the PHOENIX (Husser et al. 2013), BT-Settl and BT-Cond (Allard et al. 2012), BT-NextGen (Hauschildt et al. 1999; Allard et al. 2012), Kurucz (Kurucz 1993), and CK04 (Castelli & Kurucz 2003) stellar atmosphere models, which vary in their treatment of opacities and their assumptions regarding stellar abundances, local thermodynamic equilibrium, and convection/overshooting. ARIADNE first fits each stellar model independently, then computes the weighted average of the posterior samples of each model using the Bayesian evidence as the weight. The best-fit parameters and uncertainties are then estimated from this weighted average posterior (Vines & Jenkins 2022).

While the ARIADNE code includes a built-in framework to automatically retrieve archival photometry for any given *Gaia* star (Vines & Jenkins 2022), we chose instead to override this step and use the photometry we retrieved for our catalog. This choice was made in order to maintain self-consistency, and to avoid potential issues with the ARIADNE crossmatching routines and quality tolerances. Moreover, we found that photometry in certain bandpasses was less suitable for SED fitting due to systematic discrepancies with all of

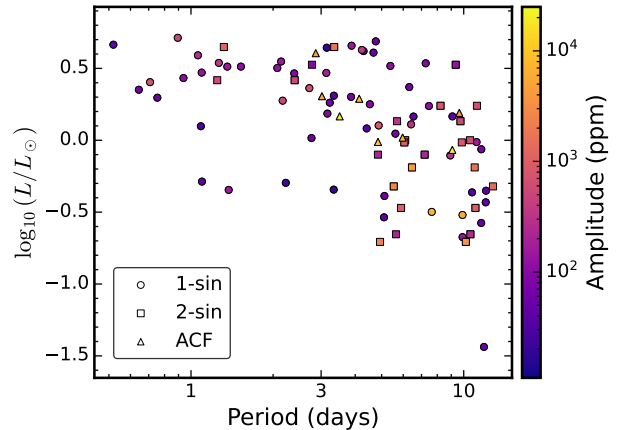


Figure 7. Stellar luminosity vs. variability period for variable stars identified in the Fetherolf et al. (2023) catalog. The colorbar indicates the relative variability amplitude, and the variability solution type is indicated by the marker shape.

the models. Specifically, we found that including the *GALEX* FUV/NUV and Strömgren u photometry would significantly degrade the quality our fits, resulting in unreliable posterior constraints and often large offsets between the models and data. Therefore, we excluded any *GALEX* FUV/NUV and Strömgren u photometry from our SED analyses. We also note that the current version of ARIADNE at the time of writing does not support fitting the mid-IR *WISE* photometry, so these data were also excluded from the analysis.

We selected priors for each fit based on the stellar parameters included in the EMSL, which are summarized in Table 3. Given some of the suspiciously narrow uncertainties associated with many of the parameters in the EMSL, we placed lower limits on the allowed variances of the normal priors used for the effective temperature, surface gravity, and metallicity in order to avoid being overly prescriptive with our prior choices. For the variance of the normal distance prior, we used the parallax angle uncertainty reported in the EMSL to calculate a corresponding distance uncertainty (as there was none reported in the EMSL). Finally, for the stellar radius we assumed a uniform prior ranging between half and twice the value of the EMSL stellar radius.

We initially included an extinction term (A_V) in our models, but we found that fitting for A_V could in some cases lead to a systematic over-estimate of effective temperature compared to the EMSL values. We attributed this result to the relatively small distances to the stars in our sample ($d < 25$ pc), which could imply negligible interstellar extinction for some targets. In these cases, including the superfluous A_V parameter could lead to over-fitting, resulting in the systematic disagreement in T_{eff} . To mitigate this issue, we ran two different version

Table 3. Summary of priors used for SED fitting.

Parameter	Prior
T_{eff} (K)	$\mathcal{N}(T_{\text{eff,EMSL}}, \max(\sigma_{T_{\text{eff,EMSL}}}, 100 \text{ K}))$
$\log g$ (cgs)	$\mathcal{N}(\log(g)_{\text{EMSL}}, \max(\sigma_{\log(g)_{\text{EMSL}}}, 0.1))$
[Fe/H]	$\mathcal{N}([\text{Fe}/\text{H}]_{\text{EMSL}}, \max(\sigma_{[\text{Fe}/\text{H}]_{\text{EMSL}}}, 0.05))$
d (pc)	$\mathcal{N}(1''/\varpi_{\text{EMSL}}, \sigma_{\varpi_{\text{EMSL}}}/\varpi_{\text{EMSL}}^2)$
R_{\star} (R_{\odot})	$\mathcal{U}(0.5R_{\star,\text{EMSL}}, 2R_{\star,\text{EMSL}})$
A_V (mag) ¹	$\mathcal{U}(0, A_{V,\text{max}})$

NOTE— $\mathcal{N}(\mu, \sigma)$ represents a normal distribution with mean μ and variance σ^2 ; $\mathcal{U}(a, b)$ represents a uniform distribution bounded between a and b .

¹ Only used for fits where A_V was used as a free parameter. $A_{V,\text{max}}$ is the maximum line-of-sight extinction from the updated SFD galactic dust map (Schlegel et al. 1998; Schlafly & Finkbeiner 2011).

of our SED fits: one with an extinction term and one without.

For both cases, we used the BMA algorithm implemented in ARIADNE (Vines & Jenkins 2022) with dynesty nested sampling (Speagle 2020) to derive best-fit parameters and posterior distributions for each of our 164 stars. We found that setting the number of live points to 1000 and using a stopping criterion of $d \log z = 0.5$ resulted in robust, converged posteriors. We then compared the Bayesian evidences of the SED models with and without interstellar extinction and selected the best-fit parameters from the model with the higher Bayesian evidence.

An example of the best-fit SED for the star HD 10476 is shown in Figure 8—note that, for plotting the SED, ARIADNE chooses the model grid that yielded the highest Bayesian evidence, but the best-fit parameters for the plotted model are estimated from the weighted average posteriors from all of the fitted models. The corresponding BMA posterior distributions for each of the fit parameters are shown in Figure 15 in Appendix B.

Lastly, we note that ARIADNE also estimates stellar age using the SED fit parameters together with the isochrones package (Morton 2015) and the MESA Isochrones and Stellar Tracks (MIST) library (Dotter 2016). While we caution that single-star isochrone fitting may be insufficient to reliably estimate stellar ages (as is apparent in the wide age uncertainties resulting from many of the ARIADNE fits), we include the estimated ages and uncertainties in our catalog as a baseline for future work investigating stellar ages more closely.

In general, we found that our SED analyses resulted in stellar parameters that were consistent with the

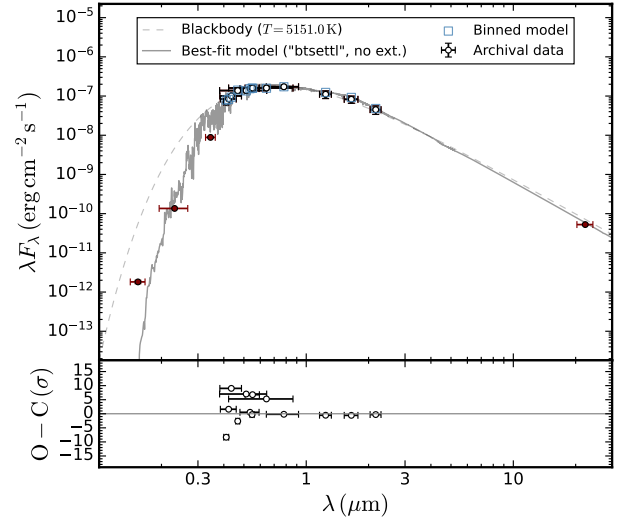


Figure 8. *Top:* Example best-fit SED model for HD 10476, computed with ARIADNE. The points with errorbars show the archival photometry, and the blue squares show the synthetic model photometry. The UV and mid-IR points (shown in maroon) were not used to compute the fit. In this case, the overplotted model with the highest Bayesian evidence was the “btsettl” stellar atmosphere with no extinction (Allard et al. 2012). The parameter posterior distributions derived from this example fit are shown in Appendix B. *Bottom:* Observed minus calculated photometry residuals, normalized to the uncertainty the data. The full set of 164 SED plots can be accessed through the online journal.

EMSL, which itself adopted values from various literature sources (Mamajek & Stapelfeldt 2023). Figure 9 shows a comparison between the T_{eff} and R_{\star} derived from our SED fits and those reported in the EMSL. We found that the SED-derived effective temperatures are all consistent with the EMSL values within 3σ , with a residual RMS of 41.8 K. For the stellar radii, we found that 94% of the SED-derived values were consistent with the EMSL within 3σ , achieving a residual RMS of $0.035 R_{\odot}$. Further discussion of these results is presented in Section 4.1

3.2. Stellar metallicity verification

While the original EMSL included stellar metallicity measurements for each star, the assumed values were selected from disparate literature sources (Mamajek & Stapelfeldt 2023). This introduced the possibility of systematic biases that depend on the particular method used to determine the stellar metallicity by each separate source catalog. The Hypatia catalog (Hinkel et al. 2014) allows for more robust stellar metallicity estimates because it combines multiple values from different source catalogs. These can subsequently be averaged together to yield more statically robust metallicity estimates.

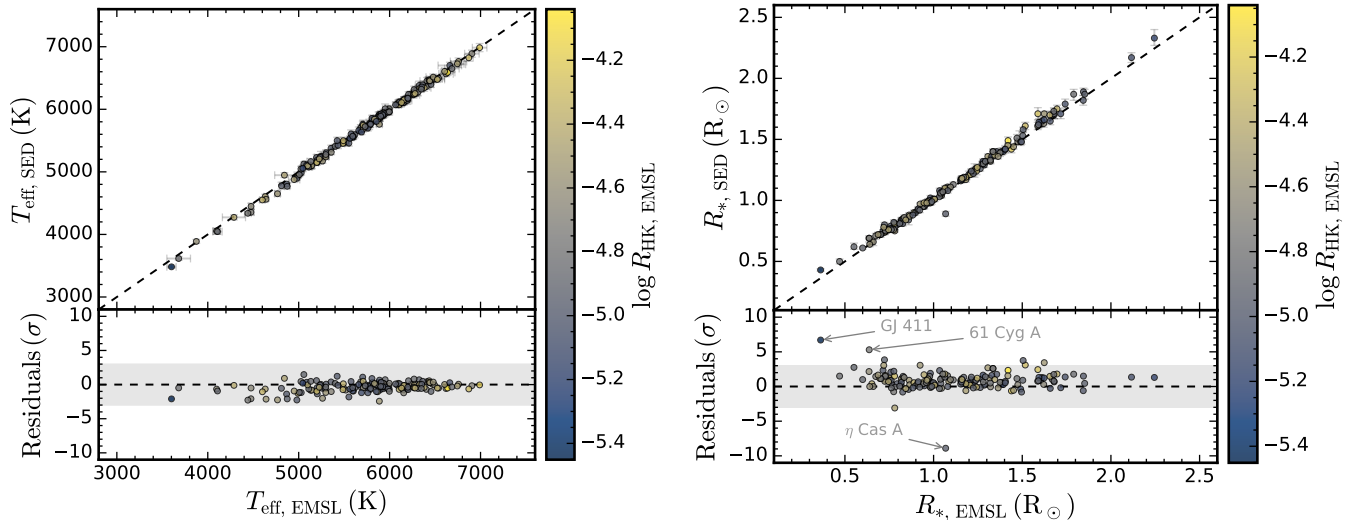


Figure 9. *Left:* Stellar effective temperature (T_{eff}) derived from the ARIADNE SED fits vs. T_{eff} reported in the EMSL table (top), along with the residuals normalized by the quadrature sum of their respective uncertainties (bottom). The black dashed line in the top panel shows a 1-to-1 correspondence, and the gray shaded box in the bottom panel highlights the region of $< 3\sigma$ discrepancy. *Right:* Same as the left-hand side, but for stellar radius (R_*).

We checked for consistency between the [Fe/H] metallicities reported in the EMSL and the average iron abundances from the Hypatia catalog. The values of [Fe/H] from the EMSL and Hypatia are plotted against one another in Figure 10. We calculated the discrepancy between the EMSL and Hypatia metallicities (in σ) by taking the quadrature sum of the EMSL metallicity uncertainty and the standard deviation of all Hypatia metallicities. All but one of the stars (GJ 380; see Section 4.3 for discussion) had metallicities from the EMSL and Hypatia that were consistent within 2σ . We calculated the RMS of the residuals to be 0.048 dex.

We also note that the metallicity uncertainties we derived from Hypatia are generally larger than those reported in the EMSL (0.065 dex median for Hypatia compared to 0.02 dex median for the EMSL) due to the systematic differences between the various Hypatia source catalogs (e.g., in stellar models, line lists, instrument resolution, instrument wavelength coverage, etc.). In principle, our more conservative metallicity uncertainties are more reliable because they take into account multiple independent analyses. However, we caution that this means that Figure 10 is not necessarily an apples-to-apples comparison, and that real trends could be blurred out due to non-astrophysical effects. We discuss these results further in Section 4.3.

4. DISCUSSION

Our updated catalog of properties of 164 promising targets for HWO includes 924 photometry measurements in 18 different bandpasses spanning from 151.6 nm to 22 μm , 1744 abundance measurements for 14 different

elements, variability metrics for 78 stars, X-ray detections for 46 stars, and flare rates for 46 stars. A more granular summary of the catalog properties is presented in Figure 11, and key physical and observable properties of the stars in our catalog are plotted in Figure 12. This catalog of stellar properties is intended to provide a starting point for future precursor and preparatory science leading up to HWO’s final mission design and eventual launch the 2040s.

4.1. Photometry and SED fits

We produced SEDs for each of the 164 stars in our sample using photometry drawn from the literature, and fit SED models to independently verify stellar parameters. Using Bayesian model averaging and 6 standard libraries of stellar atmosphere models (see Section 3.1), we derived T_{eff} , R_* , M_* , and L_* that were consistent with the literature values reported in the EMSL. A comparison of our SED fit results and literature values for T_{eff} and R_* are shown in Figure 9.

We note that the stellar radius we derived for 10 of our stars appear to be discrepant from the values reported in the literature by more than 3σ , with GJ 411, 61 Cyg A, and η Cas A having the largest disagreement. However, close inspection of the SED fits and posterior distributions did not reveal any fits with unexpectedly poor quality. We therefore attribute these discrepancies to the lack of radius uncertainties reported in the EMSL (possibly because the stellar radius is often a calculated, rather than observed, quantity). We also note that the EMSL also does not report stellar mass uncertainties. Knowing the uncertainties associated with both values

would be necessary to confidently determine whether these parameters are in fact significantly discrepant.

Furthermore, we note that the T_{eff} uncertainties from the literature may be underestimated in many cases (see, e.g., [Tayar et al. 2022](#)). The median uncertainty in T_{eff} reported in the EMSL is 20 K, which is more than a factor of two smaller than the median uncertainty we derived from SED fitting, about 47 K. Our stellar luminosity uncertainties are also about a factor of two larger than the literature values. For these reasons, we advocate that future studies of these stars adopt the slightly more conservative stellar parameters from our uniform SED fits.

4.2. Stellar SEDs and planetary habitability

Planetary habitability is critically linked to the energy output of the host star ([Buccino et al. 2007](#)). The EMSL ([Mamajek & Stapelfeldt 2023](#)) was compiled assuming the classical HZ limits (i.e., water loss and maximum greenhouse; [Kasting et al. 1993](#); [Kopparapu et al. 2013](#); [Kane et al. 2016](#); [Hill et al. 2023](#)), which were scaled by the square root of the stellar luminosity for each star. While this is a useful first approximation, the sensitivity of exoplanet habitability to the spectral energy distribution of the host star is more complex, especially for non-solar type stars which have fundamentally different SEDs. For example, two stars with the same bolometric flux will yield different effective temperatures if their SEDs are different.

Notably, UV radiation from the host star significantly influences the photochemistry of planetary atmospheres, which in turn affects surface UV environments that are connected to the origin and evolution of life (e.g., [Segura et al. 2003](#); [Buccino et al. 2007](#)). Depending on the incident UV flux, terrestrial planets orbiting different types of stars are also expected to show different atmospheric features that indicate habitability on Earth, such as H_2O , CH_4 , O_3 and N_2O ([Segura et al. 2003](#); [Kaltenegger et al. 2007](#); [Rugheimer et al. 2015a](#)). The effects of UV flux on surface and atmospheric conditions also change throughout geological time as chemical evolution modifies concentrations of ozone, methane, and hazes in the atmosphere ([Rugheimer et al. 2015b](#)).

On the other hand, the mid-IR portion of host star SEDs may have observational consequences for high-contrast direct imaging of habitable worlds. Significant mid-IR excess, for example, may indicate the presence of exozodiacal dust or warm debris disks (e.g., [Trilling et al. 2008](#)), which would degrade the quality of direct imaging and spectroscopy of HZ planets. [Mamajek & Stapelfeldt \(2023\)](#) have indicated in the EMSL which systems have previous detections of circumstellar debris

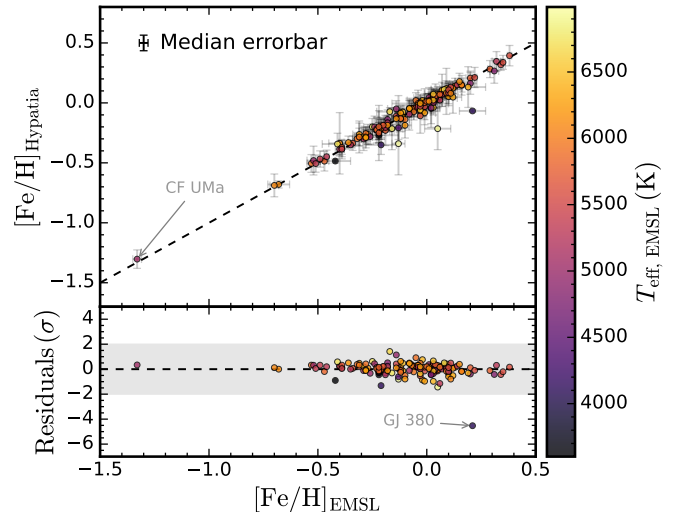


Figure 10. (Top:) Median iron abundance metallicity $[\text{Fe}/\text{H}]$ from the Hypatia Catalog vs. the $[\text{Fe}/\text{H}]$ reported in the original EMSL table, with a 1-to-1 correspondence shown by the black dashed line. The stellar effective temperature from original EMSL table is indicated by color. A representative 1σ median errorbar is shown in the upper left-hand corner. (Bottom:) The residuals between the median Hypatia and EMSL metallicities, normalized by the quadrature sum of their respective uncertainties. For the Hypatia uncertainties, we used the standard deviation of all listed values. The gray shaded box highlights the region of 2σ consistency.

disks, ranking stars with no known dust disks of any kind in tier A, stars with cold Kuiper Belt (KB) disks that were very optically thin ($L_{\text{IR}}/L_{\star} < 10^{-4}$) in tier B, and stars with any other type of disk in tier C. For completeness, we have added IR fluxes to our catalog where available, which we hope will assist in future analyses of circumstellar debris disks for this sample.

We note that currently only 33 of the stars in our sample have at least one robust space-based UV measurement, and 40 have at least one mid-IR measurement (assuming the quality cuts described in Section 2). These targets account for just 20-24% of the catalog. While UV observations of potential HWO targets are being worked on by the NASA Astrophysics Decadal Survey Precursor Science Program (ADSPSP), further work is needed to study the radiation environments of stars in our catalog more closely, particularly for stars currently lacking reliable mid-IR and UV measurements.

4.3. Stellar composition

While the EMSL catalog compiled stellar iron abundances from various sources, we have expanded this to include the averaged abundances for 14 elements from the Hypatia catalog ([Hinkel et al. 2014](#)) to facilitate future detailed modeling of planet formation for promising

HWO targets. Our catalog includes the primary building blocks of terrestrial planets (e.g., Si, Mg, Al, Fe, and Ni) and the essential ingredients for life as we know it (e.g., C, N, O, P, and S). We identified 155 (> 94%) of our stars with at least one Fe measurement in the Hypatia Catalog, and found measurements of Na, Mg, Al, Si, Ca, and Ni for at least 90% our sample. The abundances are summarized in Table 2 and Figure 4.

Host star composition is directly linked to the protoplanetary disk, which in turn controls the formation and subsequent composition of planetary building blocks (e.g., Gáspár et al. 2016; Santos et al. 2017; Adibekyan et al. 2021; Cabral et al. 2023). It is therefore commonly assumed that exoplanet composition mirrors that of the host star (although this is not always the case; see, e.g., Plotnykov & Valencia 2020; Schulze et al. 2021). While the iron abundance $[\text{Fe}/\text{H}]$ is usually known for nearby stars and often used as a proxy for scaling other stellar abundances, this information alone is insufficient for detailed interior modeling of terrestrial planets because planetary building blocks like Si, Mg, and O are understood not to scale linearly with Fe (e.g., Bitsch & Battistini 2020; Jorge et al. 2022). Figure 13 demonstrates the known non-linearity of the correlation between $[\text{Fe}/\text{H}]$ and Si, Mg, C, and O abundances in our sample.

Recent studies have implemented devolatilization models, using the detailed compositions of host stars to infer the composition and internal structure of terrestrial planets and thus demonstrating a range of plausible exo-Earth geologies (e.g., Hinkel & Unterborn 2018; Wang et al. 2022; Unterborn et al. 2023). For example, solid planet building blocks formed exterior to the water ice line depend strongly on the C/O ratio, with higher C/O in solids leading to smaller water ice fractions as more O is partitioned in gaseous CO and CO₂ (Bitsch & Battistini 2020).

The Mg/Si ratio is also important to the mineralogy of planet building blocks. According to geochemical models, planets with low Mg/Si ratios tend to cool slowly because their mantle viscosity is high and may therefore quickly lose their volatiles (Spaargaren et al. 2020). Additionally, different Mg/Si ratios shift the condensation sequence of solid planet building blocks, with lower Mg/Si ratios leading to mechanically stronger mantles and higher Mg/Si leading to weaker mantles (Jorge et al. 2022; Spaargaren et al. 2023). This can carry important consequences for lithosphere dynamics (i.e., plate tectonics, volcanism, etc.), which can drive different evolutionary pathways that affect habitability. The C/O ratio of our sample ranges from 0.16 to 1.91 (solar C/O = 0.59; Asplund et al. 2021) and the Mg/Si ratio ranges from 0.68 to 1.94 (solar Mg/Si = 1.10; As-

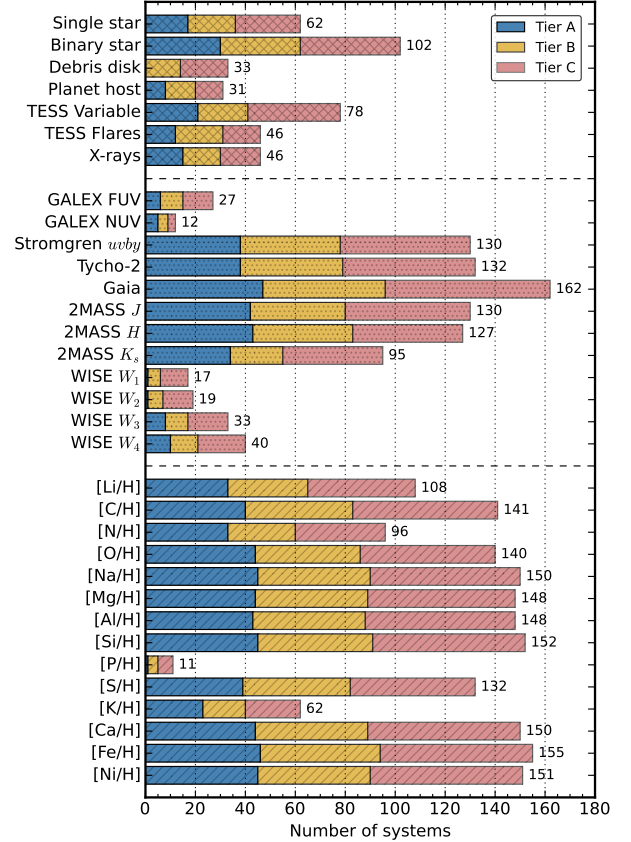


Figure 11. Bar graph showing a summary of the information in our catalog, demonstrating the (in)completeness of our knowledge about these systems. Each attribute is subdivided into the three tier levels defined by Mamajek & Stapelfeldt (2023).

plund et al. 2021). Both C/O and Mg/Si as a function of stellar metallicity are shown in Figure 14.

Moreover, the composition of the protoplanetary disk (and thus the host star) plays a role in determining the resulting system architectures of planet formation (e.g., Adibekyan et al. 2021). For example, early spectroscopy studies of exoplanet hosts demonstrated that there is a rise in the fraction of stars with planets above solar metallicity (Fischer & Valenti 2005). More recently, Tautvaišienė et al. (2022) analyzed 25 bright planet-hosts from *TESS* and showed that stars with high-mass planets tend to be more metal-rich than stars with low-mass planets. The HZ is thought to depend on planetary mass, with larger planets having wider HZs due to their smaller H₂O atmospheric column depths (Kopparapu et al. 2014). Therefore, if metal-rich stars tend to have more massive terrestrial planets, then their HZs may extend further out. This may be an important factor to consider in expanding the list of potential HWO targets.

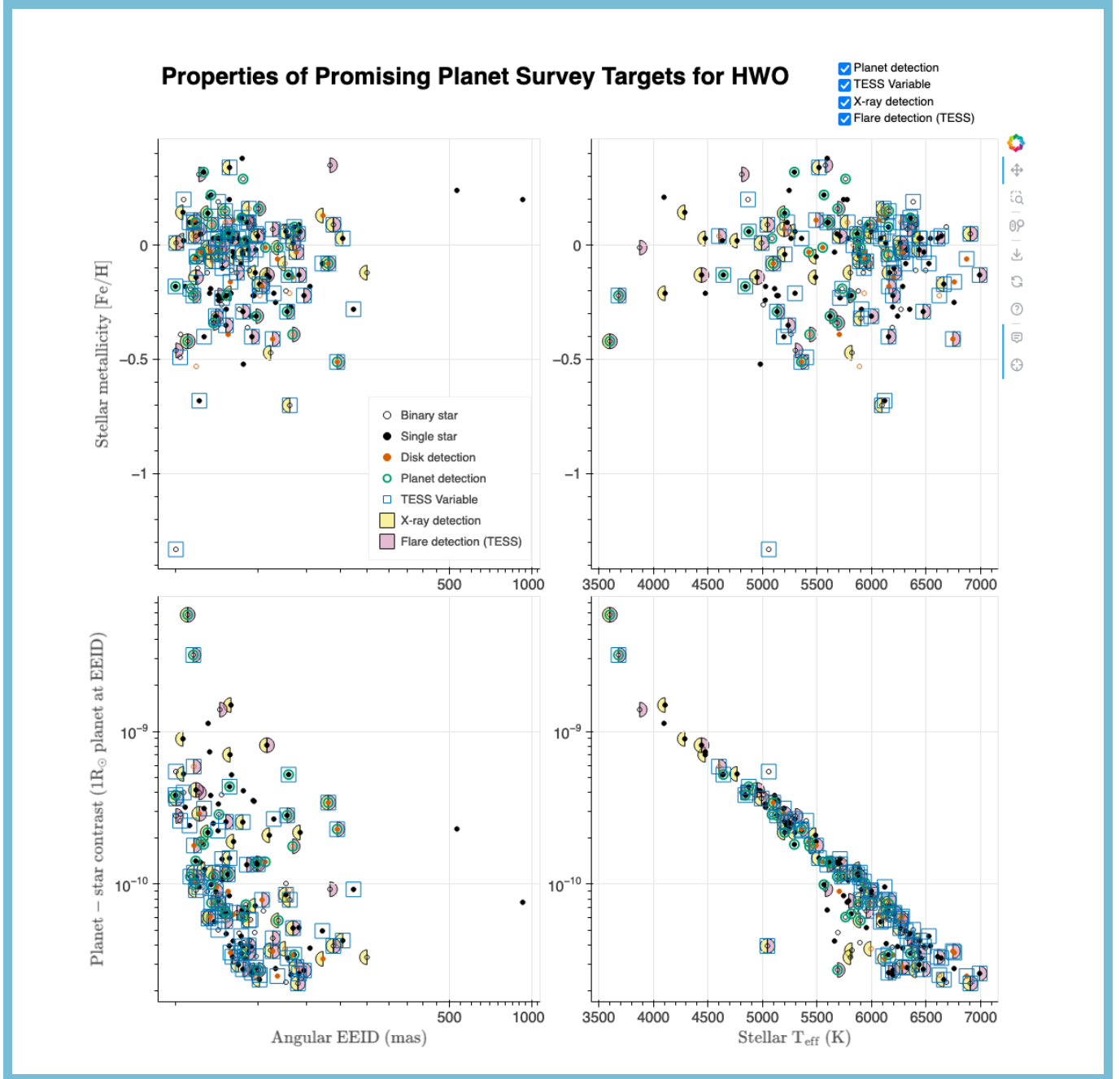


Figure 12. Physical and observable properties of stars in our catalog. Starting from the upper left-hand panel and moving clockwise, the panels show stellar metallicity vs. angular EEID, stellar metallicity vs. effective temperature, estimated planet-star contrast ratio (in R_c band) vs. effective temperature, and estimated planet-star contrast ratio vs. angular EEID. Different markers indicating stellar multiplicity, the presence of debris disks and planets, stellar variability, and flare and X-ray detections are defined in the legend. An interactive version of this figure can be accessed through the online journal.

Another consideration linked to planetary composition is the prevalence of multi-planet systems around stars of different metallicities. Compact multi-planet systems occur more frequently around stars of increasingly lower metallicities, and these systems are nearly mutually exclusive with systems containing hot Jupiters (e.g., Brewer et al. 2018). These system architectures

may complicate the dynamical stability of otherwise plausible exo-Earths, possibly excluding stable HZ orbits altogether for some systems. The star Groombridge 1830 (CF UMa), which stands out in our catalog with an extremely low metallicity of $[\text{Fe}/\text{H}] = -1.3$ (labeled in Figure 10), may therefore be a particularly interesting target. Groombridge 1830 is an early K dwarf star with

no known planetary companions and a predicted EEID angular separation of roughly 50 mas.

The abundance of bio-essential elements present in the protoplanetary disk may also influence planetary habitability. The element phosphorus, for example, is necessary for all life on Earth because it forms the backbone of DNA and RNA molecules. However, if terrestrial planets form in disks with substantially low P abundances, strong partitioning of P into to core could rule out sufficient bio-available P on the surface (Hinkel et al. 2020). Only 11 stars in our catalog ($\sim 6.7\%$) have measured P abundances, commensurate with the broader dearth of stars with P measurements in the literature—observations are challenging because the typical P absorption lines fall outside of the optical band typically used for spectroscopy (Hinkel et al. 2020). This motivates future investigations dedicated to measuring P abundances of promising HWO targets.

We note as a caution to the reader that some abundances in the Hypatia Catalog are highly uncertain, with large differences between different catalogs. We found that 12 stars in our catalog have an $[\text{Fe}/\text{H}]$ spread greater than 0.5 dex, while 2 stars, HD 38858 and δ Eri (HD 22049), have an $[\text{Fe}/\text{H}]$ spread greater than 1.0 dex. In other cases, the metallicity reported in the EMSL disagrees significantly with the average Hypatia $[\text{Fe}/\text{H}]$ abundance. For the most significant discrepancy for the star GJ 380 (HD 88230; labeled in Figure 10), the EMSL $[\text{Fe}/\text{H}]$ value was 0.21 ± 0.06 (Soubiran et al. 2022), while the mean Hypatia $[\text{Fe}/\text{H}]$ value was -0.067 (Hinkel et al. 2014). We ruled out bad crossmatching as an explanation for this discrepancy, and we verified that the range of Hypatia $[\text{Fe}/\text{H}]$ values spans from -0.08 (Woolf & Wallerstein 2005) to -0.05 (Maas et al. 2016). This suggests a possible typographical or crossmatching error with the Soubiran et al. (2022) catalog implemented in the original EMSL for this particular star.

We urge future studies using our catalog to exercise caution by checking the span of abundance measurements before assuming a particular value. In our catalog, we include the minimum and maximum Hypatia abundance values along with their literature sources to facilitate this check.

4.4. Stellar environments

We have identified 108 stars in our sample that exhibit variability, flares, and/or X-ray emission. Furthermore, the EMSL contains over 100 stars in binary systems and 4 post-main-sequence stars ($\log(g) < 4$). The stars are mostly intermediate in mass, with 66 F-type, 55 G-type, 40 K-type, and only 3 M-type stars. While this is by no means an exhaustive list of factors that may affect hab-

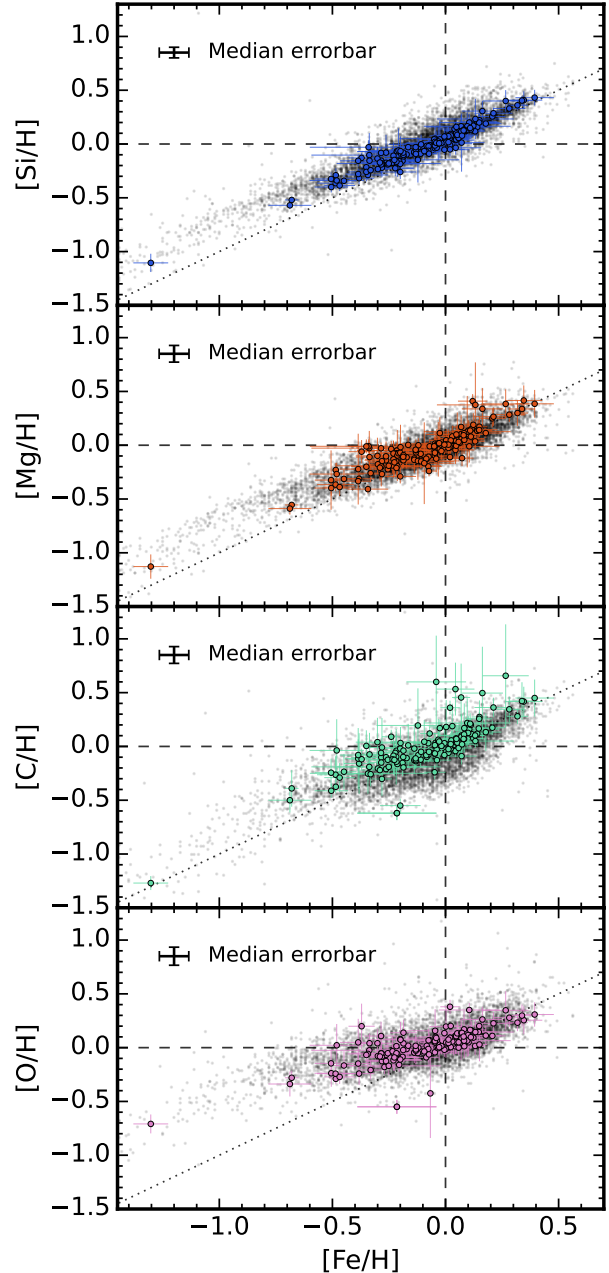


Figure 13. Abundances of silicon, magnesium, carbon, and oxygen vs. iron from the Hypatia catalog (Hinkel et al. 2014). Stars from the catalog presented in this work are shown in color. For reference, all stars with abundance measurements in the Hypatia catalog are plotted as small gray points. The vertical and horizontal dashed gray lines show solar values, and the dotted line shows a 1-to-1 correspondence. A representative median errorbar is shown in the upper left-hand corner of each subplot.

itability, it provides a useful starting point for discussing how past, present, and future stellar environments are intertwined with planetary surface conditions necessary for life.

Periodic stellar variability is often an indication of radial pulsations (typically in evolved massive stars) or rotationally-modulated brightness differences caused by photospheric heterogeneities (typically in cooler dwarf stars). In the latter case, analysis of the photometric time series can yield constraints on the rotation period and star spot coverage of the stellar photosphere. Stellar rotation has been theoretically shown to affect the limits of the HZ, especially in rapidly rotating A and F stars where the rotational forces cause the star to become oblate and develop a pole-to-equator temperature gradient (Ahlers et al. 2022). Star spot coverage on the other hand is linked to magnetic fields, and hence stellar activity, which has been extensively studied in the context of M-dwarf planet habitability (e.g., Joshi et al. 1997; Scalo et al. 2007; Gallet et al. 2017; Günther et al. 2020). Stellar flares, which are associated with high stellar activity, are high-energy transients that can emit large quantities of UV and X-ray radiation, especially in M and K dwarf stars. Flares present challenges to potential habitability because they can alter the atmospheric chemistry of terrestrial planets (primarily generating O_3 and N_2O) and expose their surfaces to high levels of ionizing radiation (e.g., Ridgway et al. 2023).

Stellar age can also present challenges to potential habitability. While the majority of stars in our sample are main-sequence stars, there are a handful of subgiant stars—notably, δ Eri (GJ 150) has the lowest surface gravity with $\log(g) = 3.78$. The HZs of post-main sequence stars move outward as the stellar luminosity increases, which can make them more accessible to direct-imaging surveys. However, stellar mass loss during the RGB and AGB phases of post-main sequence evolution can destabilize planetary orbits and drive strong stellar winds that work to erode planetary atmospheres, possibly reducing the chances of habitability (e.g., Ramirez & Kaltenegger 2016). More detailed modeling is needed to assess the importance of these effects for the few subgiant stars in our catalog.

Ultimately, a holistic assessment of each system will be necessary to select the most promising targets for HWO, informed by both observability (limited by technology) and likely scientific return (limited by precursor knowledge). Therefore, we do not attempt to narrow down the list of potential targets in this work, but rather present what is known about each system at face value in hopes that this information will be used holistically in future studies.

4.5. Data availability

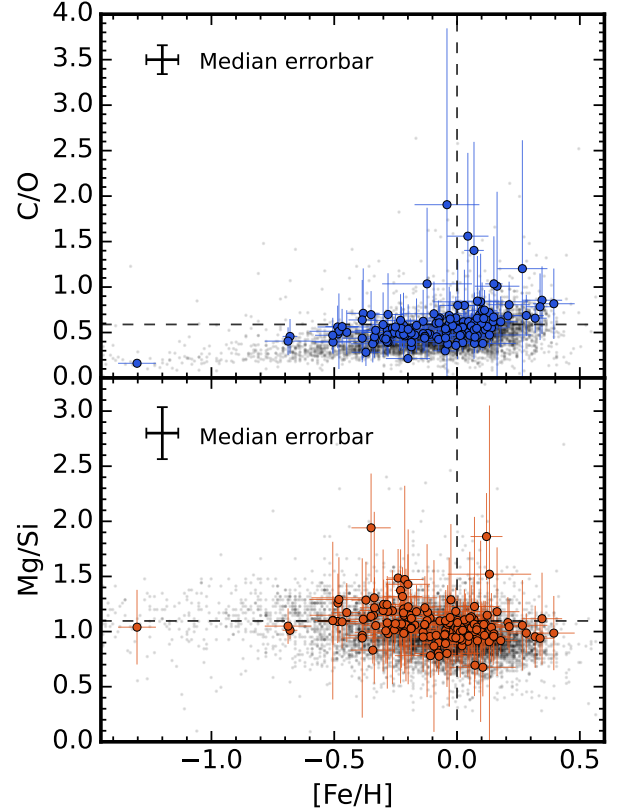


Figure 14. C/O (top) and Si/Mg (bottom) ratios vs. stellar metallicity [Fe/H] from the Hypatia catalog (Hinkel et al. 2014). Stars from the catalog presented in this work are shown in color, and all stars with abundance measurements in the Hypatia catalog are plotted as small gray points for reference. Solar metallicity and abundance ratios (C/O = 0.59, Si/Mg = 1.10; Asplund et al. 2021) are indicated by the vertical and horizontal dashed gray lines. A representative median errorbar is shown in the upper left-hand corner of each subplot.

Our catalog of 164 stars is publicly available to the community via the authors’ website¹⁵ and the online journal. A list of columns included in the current version of the catalog and their descriptions are provided in Table 4 in Appendix B. We invite the HWO community to use this catalog as a resource for their own studies.

Finally, we intend to update this catalog with additional stars and properties at a future time. Expanding the sample of potential HWO targets will enable a more comprehensive investigation in mission design trade space, as a significant portion of EMSL targets may ultimately be determined to be unsuitable for the HWO planet survey (see, e.g., Tuchow et al. 2024).

¹⁵ <https://sites.google.com/berkeley.edu/spores-hwo>

5. CONCLUSION

We have created a catalog of 164 stars that are promising targets for the Habitable Worlds Observatory, a future ~ 6 -meter class space mission capable of high-contrast direct imaging and spectroscopy (National Academies of Sciences, Engineering, and Medicine 2021). Our catalog derives from the NASA Exoplanet Exploration Program’s Mission Star List for HWO, which selected 164 nearby stars whose hypothetical ex-Earths would be most accessible to a high-contrast direct-imaging survey in terms of angular separation and planet-star contrast ratio (Mamajek & Stapelfeldt 2023). We include over 1700 individual stellar abundance measurements for 14 elements, over 900 photometry measurements spanning from 151.6 nm to 22 μm , flare rate estimates for 46 stars, variability metrics for 78 stars, and X-ray detections for 46 stars.

Bayesian analysis of the stellar spectral energy distributions yielded broadly consistent stellar parameters compared to previously published values reported in the EMSL. Iron abundances averaged from the Hypatia Catalog (Hinkel et al. 2014) are also mostly consistent with those drawn from the EMSL, but often with much more conservative uncertainties due to significant differences between the various Hypatia source catalogs. The SEDs and different compositions of the potential host stars likely have important consequences affecting their HZs and potential habitable planets, which we have discussed in detail.

We emphasize that the catalog and discussion presented here is intended to aid future work investigating these systems more closely. This work is the first in a series of forthcoming precursor science papers that will result from the NASA Astrophysics Decadal Survey Precursor Science (ADSPS) program¹⁶. Subsequent precursor science work is critical to HWO trade studies that will determine the final mission design. Throughout this work, we have hinted at future avenues toward science with HWO, including closer investigations of the stars’ high-energy and mid-IR radiation environments, more complete surveys of bio-essential element abundances, and studies of dynamical stability in systems with previously detected planets or a higher likelihood of being a compact multi-planet system.

Additionally, future work should include determining the depth of past searches for planets in these systems using archival photometry and public RV observations (e.g., Howard & Fulton 2016; Laliotis et al. 2023). A follow-up investigation of stellar variability and rotation

rates would also be useful for accurately measuring stellar ages with gyrochronology, and as a proxy for stellar activity. Lastly, as future studies begin to winnow down the list of possible HWO targets, additional stars should also be added to the list to allow for more flexibility in mission design trades. Investing in this work early on in the mission development will reduce costs while maximizing the likelihood of reaching HWO’s goal of detecting life or placing meaningful constraints on the rarity of life on other planets. The EMSL sample studied here was compiled using a somewhat limiting definition of the HZ and the assumption of only circular orbits, but this can be expanded by extending the permissible conditions for habitability and adding planets with eccentric orbits. These future pathways toward planet properties were discussed in our ADSPS program proposal.

Our catalog is publicly available, and we invite other members of the HWO community to build off of our work in future studies leading up to HWO and beyond. Ultimately, the subsequent work that follows from this catalog will play a critical role in the success of HWO and constraining the existence of life beyond the Solar System.

We acknowledge support from the NASA Astrophysics Decadal Survey Precursor Science (ADSPS) program under Grant Number 80NSSC23K1476. C.K.H. acknowledges support from the National Science Foundation (NSF) Graduate Research Fellowship Program (GRFP) under Grant No. DGE 2146752. B.A.A. acknowledges support from the Cal-Bridge Summer Research Program. This research has made use of the NASA Exoplanet Archive, which is operated by the California Institute of Technology, under contract with the National Aeronautics and Space Administration under the Exoplanet Exploration Program. The research shown here acknowledges use of the Hypatia Catalog Database, an online compilation of stellar abundance data as described in Hinkel et al. (2014), which was supported by NASA’s Nexus for Exoplanet System Science (NExSS) research coordination network and the Vanderbilt Initiative in Data-Intensive Astrophysics (VIDA). This work has made use of data from the European Space Agency (ESA) mission *Gaia* (<https://www.cosmos.esa.int/gaia>), processed by the *Gaia* Data Processing and Analysis Consortium (DPAC, <https://www.cosmos.esa.int/web/gaia/dpac/consortium>). Funding for the DPAC has been provided by national institutions, in particular the institutions participating in the *Gaia* Multilateral Agreement. This research has made use of the Washington Double Star Catalog maintained at the U.S. Naval Observatory. This research made use of Lightkurve, a Python package for Kepler and TESS

¹⁶ Funded through ADSPS22 Grant Number 80NSSC23K1476.

data analysis (Lightkurve Collaboration et al. 2018). This research has made use of the International Variable Star Index (VSX) database, operated at AAVSO, Cambridge, Massachusetts, USA.

Facilities: ADS, CDS, Exoplanet Archive, Gaia, GALEX, HIPPARCOS, MAST, TESS, WISE

Software: ARIADNE (Vines & Jenkins 2022), astropy (Astropy Collaboration et al. 2013, 2018), bokeh (Bokeh Development Team 2023), corner (Foreman-Mackey 2016), dynesty (Speagle 2020), IPython (Perez & Granger 2007), isochrones (Morton 2015), Lightkurve (Lightkurve Collaboration et al. 2018), matplotlib (Hunter 2007), NumPy (van der Walt et al. 2011; Harris et al. 2020), Pandas (Wes McKinney 2010; The Pandas Development Team 2020)

APPENDIX

A. MODIFICATIONS TO THE EMSL

Our catalog contains most of the original information included in the EMSL. However, we identified a few errors or inconsistencies that we have corrected here. These are summarized as follows.

- The EMSL contained an empty column (`eyes_lum`), which we have removed from our catalog.
- The star Toliman (α Cen B; HIP 71681) was originally flagged as a planet host in the EMSL, which we have changed here. While an Earth-mass planet candidate orbiting α Cen B was initially detected in radial velocity measurements of the system (Dumusque et al. 2012), subsequent analysis of the same data attributed the RV signal to the observation window function, thus ruling out α Cen Bb as a bona fide planet (Rajpaul et al. 2016). For this star, we have changed the `sy_pnum` column to 0 and the `sy_planets_flag` column to “N.”
- Mamajek & Stapelfeldt (2023) noted several stars in the EMSL that were previously reported to be binary, but are likely spurious (see their Appendix E). For example, the star 104 Tau (HIP 23835; WDS J05074+1839) was labeled as a “Dubious Double” in the Washington Double Star (WDS) Catalog notes, which could be attributed to a plate flaw, a positional typo in the original publication, or an optical double disappearing due to drastically different proper motions between the components (Mason et al. 2001). Lacaille 9352 (GJ 887; HIP 114046; WDS J23059–3551) was also indicated as a binary in the WDS Catalog, but subsequent RV measurements ruled out a companion star while confirming two super-Earths in the system (Jeffers et al. 2020). HD 4628 (HIP 3765; WDS J00484+0517), HD 5015 (HIP 4151; WDS J00531+6107), ζ 2 Ret (HIP 15371; WDS J03182–6230), Chara (β CVn; HIP 61317; WDS J12337+4121), and 58 Oph (HIP 86736; WDS J17434–2141) also had some previous indication of binarity in the literature, but were subsequently ruled out either by Mamajek & Stapelfeldt (2023) or previous authors. For each of these stars, we have removed the spurious data from the `wds_sep` and `wds_deltamag` columns.
- While the original EMSL included apparent V magnitudes and $B - V$ color indices, for convenience we have added a column with the isolated B magnitude. We also add a column for the B magnitude uncertainty, which we calculated by adding the V magnitude uncertainty and $B - V$ color uncertainty in quadrature.

B. ADDITIONAL FIGURES AND TABLES

This section contains additional figures and tables referenced in the main text.

REFERENCES

- Abt, H. A. 1981, ApJS, 45, 437, doi: [10.1086/190719](https://doi.org/10.1086/190719)
- . 2009, ApJS, 180, 117, doi: [10.1088/0067-0049/180/1/117](https://doi.org/10.1088/0067-0049/180/1/117)
- Adibekyan, V., Dorn, C., Sousa, S. G., et al. 2021, Science, 374, 330, doi: [10.1126/science.abg8794](https://doi.org/10.1126/science.abg8794)
- Ahlers, J. P., Fromont, E. F., Koppappu, R., Cauley, P. W., & Haqq-Misra, J. 2022, ApJ, 928, 35, doi: [10.3847/1538-4357/ac5596](https://doi.org/10.3847/1538-4357/ac5596)
- Akeson, R., Beichman, C., Kervella, P., Fomalont, E., & Benedict, G. F. 2021, AJ, 162, 14, doi: [10.3847/1538-3881/abfaff](https://doi.org/10.3847/1538-3881/abfaff)

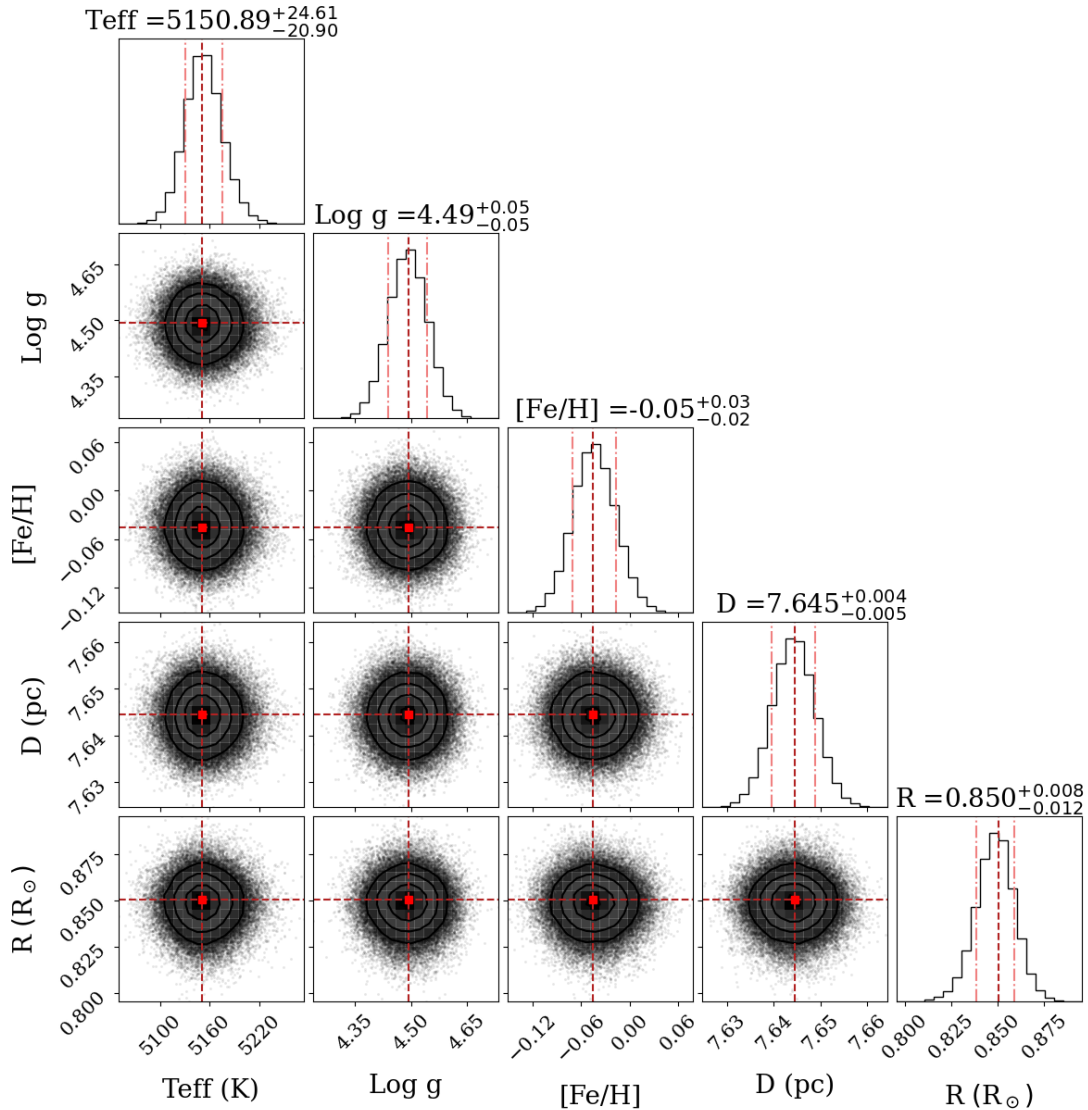


Figure 15. Posterior distributions derived from the best-fit SED model for HD 10476 shown in Figure 8. The red dots show the median posterior values, while the vertical red lines in the marginalized posterior distributions show the 16th, 50th, and 84th percentile values.

Allard, F., Homeier, D., & Freytag, B. 2012, *Philosophical Transactions of the Royal Society A: Mathematical, Physical and Engineering Sciences*, 370, 2765, doi: [10.1098/rsta.2011.0269](https://doi.org/10.1098/rsta.2011.0269)

Anders, F., Khalatyan, A., Chiappini, C., et al. 2019, *A&A*, 628, A94, doi: [10.1051/0004-6361/201935765](https://doi.org/10.1051/0004-6361/201935765)

Asplund, M., Amarsi, A. M., & Grevesse, N. 2021, *A&A*, 653, A141, doi: [10.1051/0004-6361/202140445](https://doi.org/10.1051/0004-6361/202140445)

Asplund, M., Grevesse, N., Sauval, A. J., & Scott, P. 2009, *ARA&A*, 47, 481, doi: [10.1146/annurev.astro.46.060407.145222](https://doi.org/10.1146/annurev.astro.46.060407.145222)

Astropy Collaboration, Robitaille, T. P., Tollerud, E. J., et al. 2013, *A&A*, 558, A33, doi: [10.1051/0004-6361/201322068](https://doi.org/10.1051/0004-6361/201322068)

Astropy Collaboration, Price-Whelan, A. M., Sipőcz, B. M., et al. 2018, *AJ*, 156, 123, doi: [10.3847/1538-3881/aabc4f](https://doi.org/10.3847/1538-3881/aabc4f)

Baliunas, S., Sokoloff, D., & Soon, W. 1996, *ApJL*, 457, L99, doi: [10.1086/309891](https://doi.org/10.1086/309891)

Bessel, M. S. 1990, *A&AS*, 83, 357

Bianchi, L., Shiao, B., & Thilker, D. 2017, *ApJS*, 230, 24, doi: [10.3847/1538-4365/aa7053](https://doi.org/10.3847/1538-4365/aa7053)

Bitsch, B., & Battistini, C. 2020, *A&A*, 633, A10, doi: [10.1051/0004-6361/201936463](https://doi.org/10.1051/0004-6361/201936463)

Bokeh Development Team. 2023, Bokeh: Python library for interactive visualization. <https://bokeh.org/>

Boro Saikia, S., Marvin, C. J., Jeffers, S. V., et al. 2018, *A&A*, 616, A108, doi: [10.1051/0004-6361/201629518](https://doi.org/10.1051/0004-6361/201629518)

- Boyajian, T. S., von Braun, K., van Belle, G., et al. 2012, *ApJ*, 757, 112, doi: [10.1088/0004-637X/757/2/112](https://doi.org/10.1088/0004-637X/757/2/112)
- . 2013, *ApJ*, 771, 40, doi: [10.1088/0004-637X/771/1/40](https://doi.org/10.1088/0004-637X/771/1/40)
- Brewer, J. M., Wang, S., Fischer, D. A., & Foreman-Mackey, D. 2018, *ApJL*, 867, L3, doi: [10.3847/2041-8213/aae710](https://doi.org/10.3847/2041-8213/aae710)
- Brown, E. L., Jeffers, S. V., Marsden, S. C., et al. 2022, *MNRAS*, 514, 4300, doi: [10.1093/mnras/stac1291](https://doi.org/10.1093/mnras/stac1291)
- Buccino, A. P., Lemarchand, G. A., & Mauas, P. J. D. 2007, *Icarus*, 192, 582, doi: [10.1016/j.icarus.2007.08.012](https://doi.org/10.1016/j.icarus.2007.08.012)
- Burrows, D. N., Hill, J. E., Nousek, J. A., et al. 2005, *SSRv*, 120, 165, doi: [10.1007/s11214-005-5097-2](https://doi.org/10.1007/s11214-005-5097-2)
- Cabral, N., Guilbert-Lepoutre, A., Bitsch, B., Lagarde, N., & Diakite, S. 2023, *A&A*, 673, A117, doi: [10.1051/0004-6361/202243882](https://doi.org/10.1051/0004-6361/202243882)
- Cannon, A. J., & Pickering, E. C. 1993, *VizieR Online Data Catalog*, III/135A
- Casagrande, L., Schönrich, R., Asplund, M., et al. 2011, *A&A*, 530, A138, doi: [10.1051/0004-6361/201016276](https://doi.org/10.1051/0004-6361/201016276)
- Castelli, F., & Kurucz, R. L. 2003, in *Modelling of Stellar Atmospheres*, ed. N. Piskunov, W. W. Weiss, & D. F. Gray, Vol. 210, A20. <https://arxiv.org/abs/astro-ph/0405087>
- Corbally, C. J. 1984, *ApJS*, 55, 657, doi: [10.1086/190973](https://doi.org/10.1086/190973)
- Cousins, A. W. J. 1980, *South African Astronomical Observatory Circular*, 1, 166
- Cowley, A. P. 1976, *PASP*, 88, 95, doi: [10.1086/129905](https://doi.org/10.1086/129905)
- Cowley, A. P., Hiltner, W. A., & Witt, A. N. 1967, *AJ*, 72, 1334, doi: [10.1086/110413](https://doi.org/10.1086/110413)
- Crass, J., Gaudi, B. S., Leifer, S., et al. 2021, arXiv e-prints, arXiv:2107.14291, doi: [10.48550/arXiv.2107.14291](https://doi.org/10.48550/arXiv.2107.14291)
- Cutri, R. M., Skrutskie, M. F., van Dyk, S., et al. 2003, *VizieR Online Data Catalog*, II/246
- Cutri, R. M., Wright, E. L., Conrow, T., et al. 2021, *VizieR Online Data Catalog*, II/328
- David, T. J., & Hillenbrand, L. A. 2015, *ApJ*, 804, 146, doi: [10.1088/0004-637X/804/2/146](https://doi.org/10.1088/0004-637X/804/2/146)
- Dieterich, S. B., Henry, T. J., Golimowski, D. A., Krist, J. E., & Tanner, A. M. 2012, *AJ*, 144, 64, doi: [10.1088/0004-6256/144/2/64](https://doi.org/10.1088/0004-6256/144/2/64)
- Dotter, A. 2016, *ApJS*, 222, 8, doi: [10.3847/0067-0049/222/1/8](https://doi.org/10.3847/0067-0049/222/1/8)
- Dumusque, X., Pepe, F., Lovis, C., et al. 2012, *Nature*, 491, 207, doi: [10.1038/nature11572](https://doi.org/10.1038/nature11572)
- Duncan, D. K., Vaughan, A. H., Wilson, O. C., et al. 1991, *ApJS*, 76, 383, doi: [10.1086/191572](https://doi.org/10.1086/191572)
- Eggen, O. J. 1965, *AJ*, 70, 19, doi: [10.1086/109676](https://doi.org/10.1086/109676)
- Eggenberger, P., Miglio, A., Carrier, F., Fernandes, J., & Santos, N. C. 2008, *A&A*, 482, 631, doi: [10.1051/0004-6361:20078624](https://doi.org/10.1051/0004-6361:20078624)
- ESA, . 1997a, *VizieR Online Data Catalog*, I/239
- ESA, ., ed. 1997b, *ESA Special Publication*, Vol. 1200, *The HIPPARCOS and TYCHO catalogues. Astrometric and photometric star catalogues derived from the ESA HIPPARCOS Space Astrometry Mission*
- Fetherolf, T., Pepper, J., Simpson, E., et al. 2023, *ApJS*, 268, 4, doi: [10.3847/1538-4365/acdee5](https://doi.org/10.3847/1538-4365/acdee5)
- Fischer, D. A., & Valenti, J. 2005, *ApJ*, 622, 1102, doi: [10.1086/428383](https://doi.org/10.1086/428383)
- Flesch, E. W. 2016, *PASA*, 33, e052, doi: [10.1017/pasa.2016.44](https://doi.org/10.1017/pasa.2016.44)
- . 2023, arXiv e-prints, arXiv:2308.01507, doi: [10.48550/arXiv.2308.01507](https://doi.org/10.48550/arXiv.2308.01507)
- Foreman-Mackey, D. 2016, *The Journal of Open Source Software*, 1, 24, doi: [10.21105/joss.00024](https://doi.org/10.21105/joss.00024)
- Fragoso, T. M., Bertoli, W., & Louzada, F. 2018, *International Statistical Review*, 86, 1, doi: <https://doi.org/10.1111/insr.12243>
- Fuhrmann, K. 2008, *MNRAS*, 384, 173, doi: [10.1111/j.1365-2966.2007.12671.x](https://doi.org/10.1111/j.1365-2966.2007.12671.x)
- Gaia Collaboration. 2022a, *VizieR Online Data Catalog*, I/355, doi: [10.26093/cds/vizier.1355](https://doi.org/10.26093/cds/vizier.1355)
- . 2022b, *VizieR Online Data Catalog*, I/360
- Gaia Collaboration, Prusti, T., de Bruijne, J. H. J., et al. 2016, *A&A*, 595, A1, doi: [10.1051/0004-6361/201629272](https://doi.org/10.1051/0004-6361/201629272)
- Gaia Collaboration, Brown, A. G. A., Vallenari, A., et al. 2018, *A&A*, 616, A1, doi: [10.1051/0004-6361/201833051](https://doi.org/10.1051/0004-6361/201833051)
- Gaia Collaboration, Vallenari, A., Brown, A. G. A., et al. 2023, *A&A*, 674, A1, doi: [10.1051/0004-6361/202243940](https://doi.org/10.1051/0004-6361/202243940)
- Gallet, F., Charbonnel, C., Amard, L., et al. 2017, *A&A*, 597, A14, doi: [10.1051/0004-6361/201629034](https://doi.org/10.1051/0004-6361/201629034)
- Gáspár, A., Rieke, G. H., & Ballering, N. 2016, *ApJ*, 826, 171, doi: [10.3847/0004-637X/826/2/171](https://doi.org/10.3847/0004-637X/826/2/171)
- Gaudi, B. S., Seager, S., Mennesson, B., et al. 2020, arXiv e-prints, arXiv:2001.06683, doi: [10.48550/arXiv.2001.06683](https://doi.org/10.48550/arXiv.2001.06683)
- Gliese, W., & Jahreiß, H. 1991, *Preliminary Version of the Third Catalogue of Nearby Stars, On: The Astronomical Data Center CD-ROM: Selected Astronomical Catalogs*, Vol. I; L.E. Brodzmann, S.E. Gesser (eds.), NASA/Astronomical Data Center, Goddard Space Flight Center, Greenbelt, MD
- Golovin, A., Reffert, S., Just, A., et al. 2023, *A&A*, 670, A19, doi: [10.1051/0004-6361/202244250](https://doi.org/10.1051/0004-6361/202244250)
- Gomes da Silva, J., Santos, N. C., Adibekyan, V., et al. 2021, *A&A*, 646, A77, doi: [10.1051/0004-6361/202039765](https://doi.org/10.1051/0004-6361/202039765)
- Gondoin, P. 2020, *A&A*, 641, A110, doi: [10.1051/0004-6361/202038291](https://doi.org/10.1051/0004-6361/202038291)
- Gray, R. O. 1989, *AJ*, 98, 1049, doi: [10.1086/115195](https://doi.org/10.1086/115195)

- Gray, R. O., Corbally, C. J., Garrison, R. F., et al. 2006, *AJ*, 132, 161, doi: [10.1086/504637](https://doi.org/10.1086/504637)
- Gray, R. O., Corbally, C. J., Garrison, R. F., McFadden, M. T., & Robinson, P. E. 2003, *AJ*, 126, 2048, doi: [10.1086/378365](https://doi.org/10.1086/378365)
- Gray, R. O., Napier, M. G., & Winkler, L. I. 2001, *AJ*, 121, 2148, doi: [10.1086/319956](https://doi.org/10.1086/319956)
- Günther, M. N., Zhan, Z., Seager, S., et al. 2020, *AJ*, 159, 60, doi: [10.3847/1538-3881/ab5d3a](https://doi.org/10.3847/1538-3881/ab5d3a)
- Hall, J. C., Lockwood, G. W., & Skiff, B. A. 2007, *AJ*, 133, 862, doi: [10.1086/510356](https://doi.org/10.1086/510356)
- Harris, C. R., Millman, K. J., van der Walt, S. J., et al. 2020, *Nature*, 585, 357, doi: [10.1038/s41586-020-2649-2](https://doi.org/10.1038/s41586-020-2649-2)
- Hauck, B., & Mermilliod, M. 1998, *A&AS*, 129, 431, doi: [10.1051/aas:1998195](https://doi.org/10.1051/aas:1998195)
- Hauschildt, P. H., Allard, F., & Baron, E. 1999, *The Astrophysical Journal*, 629, 865, doi: [10.1086/430754](https://doi.org/10.1086/430754)
- Henry, T. J., Soderblom, D. R., Donahue, R. A., & Baliunas, S. L. 1996, *AJ*, 111, 439, doi: [10.1086/117796](https://doi.org/10.1086/117796)
- Hill, M. L., Bott, K., Dalba, P. A., et al. 2023, *AJ*, 165, 34, doi: [10.3847/1538-3881/aca1c0](https://doi.org/10.3847/1538-3881/aca1c0)
- Hinkel, N. R., Hartnett, H. E., & Young, P. A. 2020, *ApJL*, 900, L38, doi: [10.3847/2041-8213/abb3cb](https://doi.org/10.3847/2041-8213/abb3cb)
- Hinkel, N. R., Timmes, F. X., Young, P. A., Pagano, M. D., & Turnbull, M. C. 2014, *AJ*, 148, 54, doi: [10.1088/0004-6256/148/3/54](https://doi.org/10.1088/0004-6256/148/3/54)
- Hinkel, N. R., & Unterborn, C. T. 2018, *ApJ*, 853, 83, doi: [10.3847/1538-4357/aaa5b4](https://doi.org/10.3847/1538-4357/aaa5b4)
- Hoffleit, D., & Jaschek, C. 1991, *The Bright star catalogue* (New Haven, Conn.: Yale University Observatory)
- Høg, E., Fabricius, C., Makarov, V. V., et al. 2000, *A&A*, 355, L27
- Houk, N., & Cowley, A. P. 1975, *University of Michigan Catalogue of two-dimensional spectral types for the HD stars. Volume I. Declinations -90. to -53.f0.* (University of Michigan)
- Howard, A. W., & Fulton, B. J. 2016, *PASP*, 128, 114401, doi: [10.1088/1538-3873/128/969/114401](https://doi.org/10.1088/1538-3873/128/969/114401)
- Huang, Y., Liu, X. W., Yuan, H. B., et al. 2015, *MNRAS*, 454, 2863, doi: [10.1093/mnras/stv1991](https://doi.org/10.1093/mnras/stv1991)
- Hunter, J. D. 2007, *Computing in Science and Engineering*, 9, 90, doi: [10.1109/MCSE.2007.55](https://doi.org/10.1109/MCSE.2007.55)
- Husser, T.-O., von Berg, S. W., Dreizler, S., et al. 2013, *Astronomy & Astrophysics*, 553, A6, doi: [10.1051/0004-6361/201219058](https://doi.org/10.1051/0004-6361/201219058)
- Isaacson, H., & Fischer, D. 2010, *ApJ*, 725, 875, doi: [10.1088/0004-637X/725/1/875](https://doi.org/10.1088/0004-637X/725/1/875)
- Jansen, F., Lumb, D., Altieri, B., et al. 2001, *A&A*, 365, L1, doi: [10.1051/0004-6361:20000036](https://doi.org/10.1051/0004-6361:20000036)
- Jeffers, S. V., Dreizler, S., Barnes, J. R., et al. 2020, *Science*, 368, 1477, doi: [10.1126/science.aaz0795](https://doi.org/10.1126/science.aaz0795)
- Jorge, D. M., Kamp, I. E. E., Waters, L. B. F. M., Woitke, P., & Spaargaren, R. J. 2022, *A&A*, 660, A85, doi: [10.1051/0004-6361/202142738](https://doi.org/10.1051/0004-6361/202142738)
- Joshi, M. M., Haberle, R. M., & Reynolds, R. T. 1997, *Icarus*, 129, 450, doi: [10.1006/icar.1997.5793](https://doi.org/10.1006/icar.1997.5793)
- Kaltenegger, L., Traub, W. A., & Jucks, K. W. 2007, *ApJ*, 658, 598, doi: [10.1086/510996](https://doi.org/10.1086/510996)
- Kane, S. R., Hill, M. L., Kasting, J. F., et al. 2016, *ApJ*, 830, 1, doi: [10.3847/0004-637X/830/1/1](https://doi.org/10.3847/0004-637X/830/1/1)
- Kasting, J. F., Whitmire, D. P., & Reynolds, R. T. 1993, *Icarus*, 101, 108, doi: [10.1006/icar.1993.1010](https://doi.org/10.1006/icar.1993.1010)
- Keenan, P. C., & McNeil, R. C. 1989, *ApJS*, 71, 245, doi: [10.1086/191373](https://doi.org/10.1086/191373)
- Kervella, P., Bigot, L., Gallenne, A., & Thévenin, F. 2017, *A&A*, 597, A137, doi: [10.1051/0004-6361/201629505](https://doi.org/10.1051/0004-6361/201629505)
- Kharchenko, N. V. 2001, *Kinematika i Fizika Nebesnykh Tel*, 17, 409
- King, J. R., Villarreal, A. R., Soderblom, D. R., Gulliver, A. F., & Adelman, S. J. 2003, *AJ*, 125, 1980, doi: [10.1086/368241](https://doi.org/10.1086/368241)
- Kirkpatrick, J. D., Henry, T. J., & McCarthy, Donald W., J. 1991, *ApJS*, 77, 417, doi: [10.1086/191611](https://doi.org/10.1086/191611)
- Kopparapu, R. K., Ramirez, R. M., SchottelKotte, J., et al. 2014, *ApJL*, 787, L29, doi: [10.1088/2041-8205/787/2/L29](https://doi.org/10.1088/2041-8205/787/2/L29)
- Kopparapu, R. K., Ramirez, R., Kasting, J. F., et al. 2013, *ApJ*, 765, 131, doi: [10.1088/0004-637X/765/2/131](https://doi.org/10.1088/0004-637X/765/2/131)
- Kurucz, R. 1993, *ATLAS9 Stellar Atmosphere Programs and 2 km/s grid*. Kurucz CD-ROM No. 13. Cambridge, 13
- Laliotis, K., Burt, J. A., Mamajek, E. E., et al. 2023, *AJ*, 165, 176, doi: [10.3847/1538-3881/acc067](https://doi.org/10.3847/1538-3881/acc067)
- Lee, S. G. 1984, *AJ*, 89, 702, doi: [10.1086/113569](https://doi.org/10.1086/113569)
- Lightkurve Collaboration, Cardoso, J. V. d. M., Hedges, C., et al. 2018, *Lightkurve: Kepler and TESS time series analysis in Python*, *Astrophysics Source Code Library*. <http://ascl.net/1812.013>
- Lindgren, S., & Heiter, U. 2017, *A&A*, 604, A97, doi: [10.1051/0004-6361/201730715](https://doi.org/10.1051/0004-6361/201730715)
- Luck, R. E., & Heiter, U. 2005, *AJ*, 129, 1063, doi: [10.1086/427250](https://doi.org/10.1086/427250)
- Maas, Z. G., Pilachowski, C. A., & Hinkle, K. 2016, *AJ*, 152, 196, doi: [10.3847/0004-6256/152/6/196](https://doi.org/10.3847/0004-6256/152/6/196)
- Maldonado, J., Martínez-Arnáiz, R. M., Eiroa, C., Montes, D., & Montesinos, B. 2010, *A&A*, 521, A12, doi: [10.1051/0004-6361/201014948](https://doi.org/10.1051/0004-6361/201014948)

- Mamajek, E., & Stapelfeldt, K. 2023, California Institute of Technology.
https://exoplanetarchive.ipac.caltech.edu/docs/2645_NASA_ExEP_Target_List_HWO_Documentation_2023.pdf
- Martin, D. C., Fanson, J., Schiminovich, D., et al. 2005, *ApJL*, 619, L1, doi: [10.1086/426387](https://doi.org/10.1086/426387)
- Mason, B. D., Wycoff, G. L., Hartkopf, W. I., Douglass, G. G., & Worley, C. E. 2001, *AJ*, 122, 3466, doi: [10.1086/323920](https://doi.org/10.1086/323920)
- Mermilliod, J. C. 1997, *VizieR Online Data Catalog*, II/168
- Mermilliod, J. C., Mermilliod, M., & Hauck, B. 1997, *A&AS*, 124, 349, doi: [10.1051/aas:1997197](https://doi.org/10.1051/aas:1997197)
- Meunier, N., Kretzschmar, M., Gravet, R., Mignon, L., & Delfosse, X. 2022, *A&A*, 658, A57, doi: [10.1051/0004-6361/202142120](https://doi.org/10.1051/0004-6361/202142120)
- Montes, D., González-Peinado, R., Tabernero, H. M., et al. 2018, *MNRAS*, 479, 1332, doi: [10.1093/mnras/sty1295](https://doi.org/10.1093/mnras/sty1295)
- Morgan, W. W., & Keenan, P. C. 1973, *ARA&A*, 11, 29, doi: [10.1146/annurev.aa.11.090173.000333](https://doi.org/10.1146/annurev.aa.11.090173.000333)
- Morton, T. D. 2015, *isochrones: Stellar model grid package*.
<http://ascl.net/1503.010>
- Murgas, F., Jenkins, J. S., Rojo, P., Jones, H. R. A., & Pinfield, D. J. 2013, *A&A*, 552, A27, doi: [10.1051/0004-6361/201219483](https://doi.org/10.1051/0004-6361/201219483)
- National Academies of Sciences, Engineering, and Medicine. 2021, *Pathways to Discovery in Astronomy and Astrophysics for the 2020s* (The National Academies Press), doi: [10.17226/26141](https://doi.org/10.17226/26141)
- Newton, E. R., Charbonneau, D., Irwin, J., & Mann, A. W. 2015, *ApJ*, 800, 85, doi: [10.1088/0004-637X/800/2/85](https://doi.org/10.1088/0004-637X/800/2/85)
- Pace, G. 2013, *A&A*, 551, L8, doi: [10.1051/0004-6361/201220364](https://doi.org/10.1051/0004-6361/201220364)
- Paunzen, E. 2015, *A&A*, 580, A23, doi: [10.1051/0004-6361/201526413](https://doi.org/10.1051/0004-6361/201526413)
- Perez, F., & Granger, B. E. 2007, *Computing in Science and Engineering*, 9, 21, doi: [10.1109/MCSE.2007.53](https://doi.org/10.1109/MCSE.2007.53)
- Pickles, A., & Depagne, É. 2010, *PASP*, 122, 1437, doi: [10.1086/657947](https://doi.org/10.1086/657947)
- Pietras, M., Falewicz, R., Siarkowski, M., Bicz, K., & Preś, P. 2022, *ApJ*, 935, 143, doi: [10.3847/1538-4357/ac8352](https://doi.org/10.3847/1538-4357/ac8352)
- Plotnykov, M., & Valencia, D. 2020, *MNRAS*, 499, 932, doi: [10.1093/mnras/staa2615](https://doi.org/10.1093/mnras/staa2615)
- Pye, J. P., Rosen, S., Fyfe, D., & Schröder, A. C. 2015, *A&A*, 581, A28, doi: [10.1051/0004-6361/201526217](https://doi.org/10.1051/0004-6361/201526217)
- Radick, R. R., Lockwood, G. W., Henry, G. W., Hall, J. C., & Pevtsov, A. A. 2018, *ApJ*, 855, 75, doi: [10.3847/1538-4357/aaae3](https://doi.org/10.3847/1538-4357/aaae3)
- Rajpaul, V., Aigrain, S., & Roberts, S. 2016, *MNRAS*, 456, L6, doi: [10.1093/mnrasl/slv164](https://doi.org/10.1093/mnrasl/slv164)
- Ramírez, I., Allende Prieto, C., & Lambert, D. L. 2013, *ApJ*, 764, 78, doi: [10.1088/0004-637X/764/1/78](https://doi.org/10.1088/0004-637X/764/1/78)
- Ramirez, R. M., & Kaltenegger, L. 2016, *ApJ*, 823, 6, doi: [10.3847/0004-637X/823/1/6](https://doi.org/10.3847/0004-637X/823/1/6)
- Ricker, G. R., Winn, J. N., Vanderspek, R., et al. 2014, in *Society of Photo-Optical Instrumentation Engineers (SPIE) Conference Series*, Vol. 9143, *Space Telescopes and Instrumentation 2014: Optical, Infrared, and Millimeter Wave*, ed. J. Oschmann, Jacobus M., M. Clampin, G. G. Fazio, & H. A. MacEwen, 914320, doi: [10.1117/12.2063489](https://doi.org/10.1117/12.2063489)
- Ridgway, R. J., Zamyatina, M., Mayne, N. J., et al. 2023, *MNRAS*, 518, 2472, doi: [10.1093/mnras/stac3105](https://doi.org/10.1093/mnras/stac3105)
- Rocha-Pinto, H. J., Flynn, C., Scalo, J., et al. 2004, *A&A*, 423, 517, doi: [10.1051/0004-6361:20035617](https://doi.org/10.1051/0004-6361:20035617)
- Roettenbacher, R. M., & Kane, S. R. 2017, *ApJ*, 851, 77, doi: [10.3847/1538-4357/aa991e](https://doi.org/10.3847/1538-4357/aa991e)
- Rugheimer, S., Kaltenegger, L., Segura, A., Linsky, J., & Mohanty, S. 2015a, *ApJ*, 809, 57, doi: [10.1088/0004-637X/809/1/57](https://doi.org/10.1088/0004-637X/809/1/57)
- Rugheimer, S., Segura, A., Kaltenegger, L., & Sasselov, D. 2015b, *ApJ*, 806, 137, doi: [10.1088/0004-637X/806/1/137](https://doi.org/10.1088/0004-637X/806/1/137)
- Saffe, C., Gómez, M., & Chavero, C. 2005, *A&A*, 443, 609, doi: [10.1051/0004-6361:20053452](https://doi.org/10.1051/0004-6361:20053452)
- Samus, N. N., Kazarovets, E. V., Durlevich, O. V., Kireeva, N. N., & Pastukhova, E. N. 2017, *Astronomy Reports*, 61, 80, doi: [10.1134/S1063772917010085](https://doi.org/10.1134/S1063772917010085)
- Santos, N. C., Adibekyan, V., Dorn, C., et al. 2017, *A&A*, 608, A94, doi: [10.1051/0004-6361/201731359](https://doi.org/10.1051/0004-6361/201731359)
- Scalo, J., Kaltenegger, L., Segura, A. G., et al. 2007, *Astrobiology*, 7, 85, doi: [10.1089/ast.2006.0125](https://doi.org/10.1089/ast.2006.0125)
- Schlafly, E. F., & Finkbeiner, D. P. 2011, *ApJ*, 737, 103, doi: [10.1088/0004-637X/737/2/103](https://doi.org/10.1088/0004-637X/737/2/103)
- Schlegel, D. J., Finkbeiner, D. P., & Davis, M. 1998, *ApJ*, 500, 525, doi: [10.1086/305772](https://doi.org/10.1086/305772)
- Schröder, C., Reiners, A., & Schmitt, J. H. M. M. 2009, *A&A*, 493, 1099, doi: [10.1051/0004-6361:200810377](https://doi.org/10.1051/0004-6361:200810377)
- Schulze, J. G., Wang, J., Johnson, J. A., et al. 2021, *PSJ*, 2, 113, doi: [10.3847/PSJ/abcaa8](https://doi.org/10.3847/PSJ/abcaa8)
- Schweitzer, A., Passegger, V. M., Cifuentes, C., et al. 2019, *A&A*, 625, A68, doi: [10.1051/0004-6361/201834965](https://doi.org/10.1051/0004-6361/201834965)
- Segura, A., Krellove, K., Kasting, J. F., et al. 2003, *Astrobiology*, 3, 689, doi: [10.1089/153110703322736024](https://doi.org/10.1089/153110703322736024)
- Skilling, J. 2004, in *American Institute of Physics Conference Series*, Vol. 735, *American Institute of Physics Conference Series*, ed. R. Fischer, R. Preuss, & U. V. Toussaint, 395–405, doi: [10.1063/1.1835238](https://doi.org/10.1063/1.1835238)
- Skilling, J. 2006, *Bayesian Anal.*, 1, 833, doi: [10.1214/06-BA127](https://doi.org/10.1214/06-BA127)

- Skrutskie, M. F., Cutri, R. M., Stiening, R., et al. 2006, *AJ*, 131, 1163, doi: [10.1086/498708](https://doi.org/10.1086/498708)
- Soubiran, C., Brouillet, N., & Casamiquela, L. 2022, *A&A*, 663, A4, doi: [10.1051/0004-6361/202142409](https://doi.org/10.1051/0004-6361/202142409)
- Spaargaren, R. J., Ballmer, M. D., Bower, D. J., Dorn, C., & Tackley, P. J. 2020, *A&A*, 643, A44, doi: [10.1051/0004-6361/202037632](https://doi.org/10.1051/0004-6361/202037632)
- Spaargaren, R. J., Wang, H. S., Mojzsis, S. J., Ballmer, M. D., & Tackley, P. J. 2023, *ApJ*, 948, 53, doi: [10.3847/1538-4357/acac7d](https://doi.org/10.3847/1538-4357/acac7d)
- Speagle, J. S. 2020, *MNRAS*, 493, 3132, doi: [10.1093/mnras/staa278](https://doi.org/10.1093/mnras/staa278)
- Stanford-Moore, S. A., Nielsen, E. L., De Rosa, R. J., Macintosh, B., & Czekala, I. 2020, *ApJ*, 898, 27, doi: [10.3847/1538-4357/ab9a35](https://doi.org/10.3847/1538-4357/ab9a35)
- Stassun, K. G., Oelkers, R. J., Pepper, J., et al. 2018, *AJ*, 156, 102, doi: [10.3847/1538-3881/aad050](https://doi.org/10.3847/1538-3881/aad050)
- Stassun, K. G., Oelkers, R. J., Paegert, M., et al. 2019, *AJ*, 158, 138, doi: [10.3847/1538-3881/ab3467](https://doi.org/10.3847/1538-3881/ab3467)
- Takeda, G., Ford, E. B., Sills, A., et al. 2007, *ApJS*, 168, 297, doi: [10.1086/509763](https://doi.org/10.1086/509763)
- Takeda, Y., Ohkubo, M., Sato, B., Kambe, E., & Sadakane, K. 2005, *PASJ*, 57, 27, doi: [10.1093/pasj/57.1.27](https://doi.org/10.1093/pasj/57.1.27)
- Tautvaišienė, G., Mikolaitis, Š., Drazdauskas, A., et al. 2022, *ApJS*, 259, 45, doi: [10.3847/1538-4365/ac50b5](https://doi.org/10.3847/1538-4365/ac50b5)
- Tayar, J., Claytor, Z. R., Huber, D., & van Saders, J. 2022, *ApJ*, 927, 31, doi: [10.3847/1538-4357/ac4bbc](https://doi.org/10.3847/1538-4357/ac4bbc)
- The LUVUOIR Team. 2019, arXiv e-prints, arXiv:1912.06219, doi: [10.48550/arXiv.1912.06219](https://doi.org/10.48550/arXiv.1912.06219)
- The Pandas Development Team. 2020, pandas-dev/pandas: Pandas, latest, Zenodo, doi: [10.5281/zenodo.3509134](https://doi.org/10.5281/zenodo.3509134)
- Torres, C. A. O., Quast, G. R., da Silva, L., et al. 2006, *A&A*, 460, 695, doi: [10.1051/0004-6361:20065602](https://doi.org/10.1051/0004-6361:20065602)
- Trilling, D. E., Bryden, G., Beichman, C. A., et al. 2008, *ApJ*, 674, 1086, doi: [10.1086/525514](https://doi.org/10.1086/525514)
- Tuchow, N., Stark, C., & Mamajek, E. 2024, arXiv e-prints, arXiv:2402.08038, doi: [10.48550/arXiv.2402.08038](https://doi.org/10.48550/arXiv.2402.08038)
- Twarog, B. A., & Anthony-Twarog, B. J. 1995, *AJ*, 109, 2828, doi: [10.1086/117490](https://doi.org/10.1086/117490)
- Unterborn, C. T., Desch, S. J., Haldemann, J., et al. 2023, *ApJ*, 944, 42, doi: [10.3847/1538-4357/aca3b](https://doi.org/10.3847/1538-4357/aca3b)
- Valenti, J. A., & Fischer, D. A. 2005, *ApJS*, 159, 141, doi: [10.1086/430500](https://doi.org/10.1086/430500)
- van der Walt, S., Colbert, S. C., & Varoquaux, G. 2011, *Computing in Science and Engineering*, 13, 22, doi: [10.1109/MCSE.2011.37](https://doi.org/10.1109/MCSE.2011.37)
- van Leeuwen, F. 2007, *A&A*, 474, 653, doi: [10.1051/0004-6361:20078357](https://doi.org/10.1051/0004-6361:20078357)
- Vican, L. 2012, *AJ*, 143, 135, doi: [10.1088/0004-6256/143/6/135](https://doi.org/10.1088/0004-6256/143/6/135)
- Vines, J. I., & Jenkins, J. S. 2022, *MNRAS*, 513, 2719, doi: [10.1093/mnras/stac956](https://doi.org/10.1093/mnras/stac956)
- Voges, W., Aschenbach, B., Boller, T., et al. 1999, *A&A*, 349, 389, doi: [10.48550/arXiv.astro-ph/9909315](https://doi.org/10.48550/arXiv.astro-ph/9909315)
- Wang, H. S., Quanz, S. P., Yong, D., et al. 2022, *MNRAS*, 513, 5829, doi: [10.1093/mnras/stac1119](https://doi.org/10.1093/mnras/stac1119)
- Weisskopf, M. C., Tananbaum, H. D., Van Speybroeck, L. P., & O'Dell, S. L. 2000, in *Society of Photo-Optical Instrumentation Engineers (SPIE) Conference Series*, Vol. 4012, X-Ray Optics, Instruments, and Missions III, ed. J. E. Truemper & B. Aschenbach, 2–16, doi: [10.1117/12.391545](https://doi.org/10.1117/12.391545)
- Wes McKinney. 2010, in *Proceedings of the 9th Python in Science Conference*, ed. Stéfan van der Walt & Jarrod Millman, 56 – 61, doi: [10.25080/Majora-92bf1922-00a](https://doi.org/10.25080/Majora-92bf1922-00a)
- Wolf, V. M., & Wallerstein, G. 2005, *MNRAS*, 356, 963, doi: [10.1111/j.1365-2966.2004.08515.x](https://doi.org/10.1111/j.1365-2966.2004.08515.x)
- Wright, E. L., Eisenhardt, P. R. M., Mainzer, A. K., et al. 2010, *AJ*, 140, 1868, doi: [10.1088/0004-6256/140/6/1868](https://doi.org/10.1088/0004-6256/140/6/1868)
- Wright, J. T., Marcy, G. W., Butler, R. P., & Vogt, S. S. 2004, *ApJS*, 152, 261, doi: [10.1086/386283](https://doi.org/10.1086/386283)
- Yang, Z., Zhang, L., Meng, G., et al. 2023, *A&A*, 669, A15, doi: [10.1051/0004-6361/202142710](https://doi.org/10.1051/0004-6361/202142710)
- Yee, S. W., Petigura, E. A., & von Braun, K. 2017, *ApJ*, 836, 77, doi: [10.3847/1538-4357/836/1/77](https://doi.org/10.3847/1538-4357/836/1/77)
- Zorec, J., & Royer, F. 2012, *A&A*, 537, A120, doi: [10.1051/0004-6361/201117691](https://doi.org/10.1051/0004-6361/201117691)

Table 4. Column definitions.

Column name	Unit	Description	EMSL	Ref. #
<code>tic_id</code>		TIC designation in the TESS Input Catalog.	Y	86
<code>hip_name</code>		HIP designation in the Hipparcos Catalog.	Y	26
<code>hip_compname</code>		Component letters provided for when multiple stars are associated with the HIP entry (following CCDM, WDS, or SIMBAD).	Y	62
<code>hd_name</code>		HD designation in the Henry Draper Catalog.	Y	12
<code>hr_name</code>		HR designation in the Bright Star Catalog, 5th Edition.	Y	48
<code>gj_name</code>		GJ designation in the Preliminary Version of the Third Catalogue of Nearby Stars (CNS3) or Fifth Catalogue of Nearby Stars (CNS5).	Y	36, 37
<code>constellation</code>		Constellation ID using Greek letters or numbers following the Bright Star Catalog, 5th Edition, or the Variable star ID from the General Catalogue of Variable Stars (GCVS), Version 5.1. The Greek letter abbreviations follow SIMBAD and the 3-letter constellation abbreviations follow IAU.	Y	48, 80
<code>hostname</code>		Common star ID, usually either (in order) IAU proper name, constellation ID (Greek letter, number, or variable star) written out in genitive form with the Greek letter written in the Latin alphabet, or ID from the HD, HR, or GJ catalogs. In some cases, the discovery ID is used for notable stars (e.g., Lacaille 8760).	Y	62
<code>sy_dist</code>	pc	System distance d , calculated as $(1000 \text{ mas}/\varpi)$.	Y	62
<code>sy_plx</code>	mas	System parallax ϖ .	Y	3, 31, 32, 93
<code>sy_plxerr</code>	mas	Uncertainty in ϖ .	Y	3, 31, 32, 93
<code>sy_plx_bibcode</code>		Reference bibcode for ϖ .	Y	62
<code>ra</code>	deg	Right ascension (ICRS J2000).	Y	62
<code>dec</code>	deg	Declination (ICRS J2000).	Y	62
<code>sy_vmag</code>	mag	Johnson V apparent magnitude.	Y	24, 26, 45, 55, 64, 65, 91
<code>sy_vmagerr</code>	mag	Uncertainty in the Johnson V apparent magnitude.	Y	24, 26, 45, 55, 64, 65, 91
<code>sy_vmag_bibcode</code>		Reference bibcode for the Johnson V apparent magnitude.	Y	62
<code>sy_bvmag</code>	mag	Johnson $B - V$ color index.	Y	23, 26, 32, 55, 64, 65
<code>sy_bvmagerr</code>	mag	Uncertainty in the Johnson $B - V$ color index.	Y	23, 26, 32, 55, 64, 65
<code>sy_bvmag_bibcode</code>		Reference bibcode for the Johnson $B - V$ color index.	Y	62
<code>sy_rcmag*</code>	mag	Apparent Cousins R_c magnitude.	Y	6, 15, 33, 51, 73
<code>sy_rcmag_bibcode*</code>		Reference bibcode for the apparent Cousins R_c magnitude.	Y	62

Table 4 *continued*

Table 4 (*continued*)

Column name	Unit	Description	EMSL	Ref. #
<code>st_spectype</code>		Stellar spectral type.	Y	1, 2, 14, 16, 17, 21, 40, 41, 42, 43, 50, 53, 57, 58, 68, 90
<code>st_spectype_bibcode</code>		Reference bibcode for the spectral type.	Y	62
<code>st_teff</code>	K	Stellar effective temperature T_{eff} .	Y	13, 31, 32, 67, 70, 77, 82, 83, 86, 87, 92, 95, 99
<code>st_tefferr</code>	K	Uncertainty in T_{eff} .	Y	13, 31, 32, 67, 70, 77, 82, 83, 86, 87, 92, 95, 99
<code>st_teff_bibcode</code>		Reference bibcode for T_{eff} .	Y	62
<code>st_lum</code>	dex	Logarithmic stellar bolometric luminosity normalized to solar, $\log_{10}(L_{\text{bol}}/L_{\odot})$.	Y	9, 10, 11, 31, 32, 54, 85, 86, 92, 98
<code>st_lumerr</code>	dex	Uncertainty in $\log_{10}(L_{\text{bol}}/L_{\odot})$.	Y	9, 10, 11, 31, 32, 54, 85, 86, 92, 98
<code>st_lum_bibcode</code>		Reference bibcode for $\log_{10}(L_{\text{bol}}/L_{\odot})$.	Y	62
<code>st_rad</code>	R_{\odot}	Stellar radius R_{\star} .	Y	62
<code>st_diam</code>	mas	Stellar angular diameter.	Y	62
<code>st_mass</code>	M_{\odot}	Stellar mass M_{\star} .	Y	62
<code>st_met</code>	dex	Stellar metallicity (\log_{10} of the ratio of iron or average of metals to hydrogen, normalized to solar; generally either [Fe/H] or [M/H]).	Y	32, 35, 59, 60, 77, 83, 87, 92, 95, 98
<code>st_meterr</code>	dex	Uncertainty in stellar metallicity.	Y	32, 35, 59, 60, 77, 83, 87, 92, 95, 98
<code>st_met_bibcode</code>		Reference bibcode for stellar metallicity.	Y	62
<code>st_metratio</code>		Type of stellar metallicity (generally either [Fe/H] or [M/H]).	Y	62
<code>st_logg</code>	dex	Logarithmic stellar surface gravity, $\log g$, in units of $\log_{10}(\text{cm s}^{-2})$.	Y	4, 20, 30, 32, 77, 82, 83, 86, 87, 88, 92, 95, 98
<code>st_loggerr</code>	dex	Uncertainty in $\log g$.	Y	4, 20, 30, 32, 77, 82, 83, 86, 87, 88, 92, 95, 98
<code>st_logg_bibcode</code>		Reference bibcode for $\log g$.	Y	62
<code>st_log_rhk</code>	dex	Stellar Ca II H & K chromospheric activity index, $\log_{10}(R'_{\text{HK}})$.	Y	5, 8, 22, 38, 39, 42, 43, 44, 46, 52, 56, 61, 66, 69, 71, 76, 78, 79, 81, 84, 94, 96

Table 4 *continued*

Table 4 (continued)

Column name	Unit	Description	EMSL	Ref. #
st_log_rhk_bibcode		Reference bibcode for $\log_{10}(R'_{\text{HK}})$.	Y	62
st_eei_orbsep	au	Earth equivalent instellation distance (EEID), calculated as $\sqrt{L_{\text{bol}}/L_{\odot}}$.	Y	62
st_eei_angsep	mas	Angular EEID, calculated as EEID (in au) divided by d (in pc).	Y	62
st_eei_orbper	days	Calculated orbital period for a planet at the EEID.	Y	62
st_etwin_bratio		Calculated planet-star brightness ratio, C , for a $1 R_{\oplus}$ planet at EEID with an assumed geometric albedo of 0.2 at a phase angle of 91 degrees.	Y	62
st_etwin_rcmag	mag	Calculated apparent Cousins R_c magnitude for a $1 R_{\oplus}$ planet at EEID with an assumed geometric albedo of 0.2 at a phase angle of 91 degrees, calculated as $R_{c,\text{planet}} = R_{c,*} - 2.5 \log_{10}(C)$.	Y	62
st_etwin_rvamp	cm s^{-2}	Calculated radial velocity amplitude of the star induced by a $1 M_{\oplus}$ planet at EEID.	Y	62
st_etwin_astamp	μas	Calculated astrometric amplitude of the star induced by a $1 M_{\oplus}$ planet at EEID.	Y	62
wds_designation		WDS designation for multiple star systems in the Washington Double Star (WDS) Catalog.	Y	63
wds_comp		Component for star in WDS multiple system.	Y	63
wds_sep	arcsec	Angular separation between star and other WDS component.	Y	63
wds_deltamag	mag	Magnitude difference between target star and other WDS component star.	Y	63
sy_disks_flag		Flag if star has an infrared excess indicative of a dust disk, as measured by IRAS, Spitzer, Herschel, WISE, or LBTI (Y=yes, N=no).	Y	62
sy_disks_flag_bibcode		Reference bibcode for dust disk.	Y	62
sy_planets_flag		Flag if star has one or more confirmed exoplanets in the NASA Exoplanet Archive (Y=yes, N=no).	Y	62
sy_pnum		Number of confirmed exoplanets in the system from the NASA Exoplanet Archive.	Y	62
target_group		Tier group for target star (A, B, C).	Y	62
sy_bmag	mag	Apparent Johnson B magnitude, derived from the 3 $B - V$ color index.	N	89
sy_bmagerr	mag	Uncertainty in the apparent Johnson B magnitude.	N	89
tic_id_number		TIC ID number.	N	89
gaia_dr2_id		Cross-matched Gaia DR2 ID.	N	86
gaia_dr3_id		Cross-matched Gaia DR3 ID.	N	34
gaia_Gmag	mag	Gaia G magnitude.	N	34
gaia_Gmagerr	mag	Gaia G magnitude uncertainty.	N	34
gaia_BPmag	mag	Gaia G_{BP} magnitude.	N	34
gaia_BPmagerr	mag	Gaia G_{BP} magnitude uncertainty.	N	34
gaia_RPmag	mag	Gaia G_{RP} magnitude.	N	34

Table 4 continued

Table 4 (continued)

Column name	Unit	Description	EMSL	Ref. #
gaia_RPmagerr	mag	Gaia G_{RP} magnitude uncertainty.	N	34
all_wise_id		Cross-matched AllWISE ID.	N	34
wise_W1mag	mag	AllWISE W_1 magnitude.	N	19
wise_W1magerr	mag	AllWISE W_1 magnitude uncertainty.	N	19
wise_W2mag	mag	AllWISE W_2 magnitude.	N	19
wise_W2magerr	mag	AllWISE W_2 magnitude uncertainty.	N	19
wise_W3mag	mag	AllWISE W_3 magnitude.	N	19
wise_W3magerr	mag	AllWISE W_3 magnitude uncertainty.	N	19
wise_W4mag	mag	AllWISE W_4 magnitude.	N	19
wise_W4magerr	mag	AllWISE W_4 magnitude uncertainty.	N	19
two_mass_id		Cross-matched 2MASS ID.	N	34
two_mass_Jmag	mag	2MASS J magnitude.	N	18
two_mass_Jmagerr	mag	2MASS J magnitude uncertainty.	N	18
two_mass_Hmag	mag	2MASS H magnitude.	N	18
two_mass_Hmagerr	mag	2MASS H magnitude uncertainty.	N	18
two_mass_Ksmag	mag	2MASS K_s magnitude.	N	18
two_mass_Ksmagerr	mag	2MASS K_s magnitude uncertainty.	N	18
tycho2_id		Cross-matched Tycho-2 ID.	N	34
tycho2_BTmag	mag	Tycho-2 B_T magnitude.	N	49
tycho2_BTmagerr	mag	Tycho-2 B_T magnitude uncertainty.	N	49
tycho2_VTmag	mag	Tycho-2 V_T magnitude.	N	49
tycho2_VTmagerr	mag	Tycho-2 V_T magnitude uncertainty.	N	49
stromgren_umag	mag	Strömgren u magnitude.	N	72
stromgren_umagerr	mag	Strömgren u magnitude uncertainty.	N	72
stromgren_vmag	mag	Strömgren v magnitude.	N	72
stromgren_vmagerr	mag	Strömgren v magnitude uncertainty.	N	72
stromgren_bmag	mag	Strömgren b magnitude.	N	72
stromgren_bmagerr	mag	Strömgren b magnitude uncertainty.	N	72
stromgren_ymag	mag	Strömgren y magnitude.	N	72
stromgren_ymagerr	mag	Strömgren y magnitude uncertainty.	N	72
galex_name		Cross-matched GALEX identifier.	N	89
galex_FUVmag	mag	GALEX FUV magnitude.	N	7
galex_FUVmagerr	mag	GALEX FUV magnitude uncertainty.	N	7
galex_NUVmag	mag	GALEX NUV magnitude.	N	7
galex_NUVmagerr	mag	GALEX NUV magnitude uncertainty.	N	7
hypatia_Li_mean	dex	Mean lithium abundance [Li/H] from the Hypatia Catalog.	N	47
hypatia_Li_err [†]	dex	Lithium abundance uncertainty, calculated as the standard deviation of all [Li/H] values from the Hypatia Catalog.	N	47
hypatia_Li_nval		Number of [Li/H] measurements in the Hypatia Catalog.	N	47

Table 4 continued

Table 4 (*continued*)

Column name	Unit	Description	EMSL	Ref. #
hypatia_Li_min	dex	Minimum [Li/H] in the Hypatia Catalog.	N	47
hypatia_Li_minref		Literature reference for the minimum [Li/H] measurement in the Hypatia Catalog.	N	47
hypatia_Li_max	dex	Maximum [Li/H] in the Hypatia Catalog.	N	47
hypatia_Li_maxref		Literature reference for the maximum [Li/H] measurement in the Hypatia Catalog.	N	47
hypatia_C_mean	dex	Mean carbon abundance [C/H] from the Hypatia Catalog.	N	47
hypatia_C_err [†]	dex	Carbon abundance uncertainty, calculated as the standard deviation of all [C/H] values from the Hypatia Catalog.	N	47
hypatia_C_nval		Number of [C/H] measurements in the Hypatia Catalog.	N	47
hypatia_C_min	dex	Minimum [C/H] in the Hypatia Catalog.	N	47
hypatia_C_minref		Literature reference for the minimum [C/H] measurement in the Hypatia Catalog.	N	47
hypatia_C_max	dex	Maximum [C/H] in the Hypatia Catalog.	N	47
hypatia_C_maxref		Literature reference for the maximum [C/H] measurement in the Hypatia Catalog.	N	47
hypatia_N_mean	dex	Mean nitrogen abundance [N/H] from the Hypatia Catalog.	N	47
hypatia_N_err [†]	dex	Nitrogen abundance uncertainty, calculated as the standard deviation of all [N/H] values from the Hypatia Catalog.	N	47
hypatia_N_nval		Number of [N/H] measurements in the Hypatia Catalog.	N	47
hypatia_N_min	dex	Minimum [N/H] in the Hypatia Catalog.	N	47
hypatia_N_minref		Literature reference for the minimum [N/H] measurement in the Hypatia Catalog.	N	47
hypatia_N_max	dex	Maximum [N/H] in the Hypatia Catalog.	N	47
hypatia_N_maxref		Literature reference for the maximum [N/H] measurement in the Hypatia Catalog.	N	47
hypatia_O_mean	dex	Mean oxygen abundance [O/H] from the Hypatia Catalog.	N	47
hypatia_O_err [†]	dex	Oxygen abundance uncertainty, calculated as the standard deviation of all [O/H] values from the Hypatia Catalog.	N	47
hypatia_O_nval		Number of [O/H] measurements in the Hypatia Catalog.	N	47
hypatia_O_min	dex	Minimum [O/H] in the Hypatia Catalog.	N	47
hypatia_O_minref		Literature reference for the minimum [O/H] measurement in the Hypatia Catalog.	N	47
hypatia_O_max	dex	Maximum [O/H] in the Hypatia Catalog.	N	47
hypatia_O_maxref		Literature reference for the maximum [O/H] measurement in the Hypatia Catalog.	N	47
hypatia_Na_mean	dex	Mean sodium abundance [Na/H] from the Hypatia Catalog.	N	47

Table 4 *continued*

Table 4 (*continued*)

Column name	Unit	Description	EMSL	Ref. #
hypatia_Na_err [†]	dex	Sodium abundance uncertainty, calculated as the standard deviation of all [Na/H] values from the Hypatia Catalog.	N	47
hypatia_Na_nval		Number of [Na/H] measurements in the Hypatia Catalog.	N	47
hypatia_Na_min	dex	Minimum [Na/H] in the Hypatia Catalog.	N	47
hypatia_Na_minref		Literature reference for the minimum [Na/H] measurement in the Hypatia Catalog.	N	47
hypatia_Na_max	dex	Maximum [Na/H] in the Hypatia Catalog.	N	47
hypatia_Na_maxref		Literature reference for the maximum [Na/H] measurement in the Hypatia Catalog.	N	47
hypatia_Mg_mean	dex	Mean magnesium abundance [Mg/H] from the Hypatia Catalog.	N	47
hypatia_Mg_err [†]	dex	Magnesium abundance uncertainty, calculated as the standard deviation of all [Mg/H] values from the Hypatia Catalog.	N	47
hypatia_Mg_nval		Number of [Mg/H] measurements in the Hypatia Catalog.	N	47
hypatia_Mg_min	dex	Minimum [Mg/H] in the Hypatia Catalog.	N	47
hypatia_Mg_minref		Literature reference for the minimum [Mg/H] measurement in the Hypatia Catalog.	N	47
hypatia_Mg_max	dex	Maximum [Mg/H] in the Hypatia Catalog.	N	47
hypatia_Mg_maxref		Literature reference for the maximum [Mg/H] measurement in the Hypatia Catalog.	N	47
hypatia_Al_mean	dex	Mean aluminum abundance [Al/H] from the Hypatia Catalog.	N	47
hypatia_Al_err [†]	dex	Aluminum abundance uncertainty, calculated as the standard deviation of all [Al/H] values from the Hypatia Catalog.	N	47
hypatia_Al_nval		Number of [Al/H] measurements in the Hypatia Catalog.	N	47
hypatia_Al_min	dex	Minimum [Al/H] in the Hypatia Catalog.	N	47
hypatia_Al_minref		Literature reference for the minimum [Al/H] measurement in the Hypatia Catalog.	N	47
hypatia_Al_max	dex	Maximum [Al/H] in the Hypatia Catalog.	N	47
hypatia_Al_maxref		Literature reference for the maximum [Al/H] measurement in the Hypatia Catalog.	N	47
hypatia_Si_mean	dex	Mean silicon abundance [Si/H] from the Hypatia Catalog.	N	47
hypatia_Si_err [†]	dex	Silicon abundance uncertainty, calculated as the standard deviation of all [Si/H] values from the Hypatia Catalog.	N	47
hypatia_Si_nval		Number of [Si/H] measurements in the Hypatia Catalog.	N	47
hypatia_Si_min	dex	Minimum [Si/H] in the Hypatia Catalog.	N	47
hypatia_Si_minref		Literature reference for the minimum [Si/H] measurement in the Hypatia Catalog.	N	47
hypatia_Si_max	dex	Maximum [Si/H] in the Hypatia Catalog.	N	47
hypatia_Si_maxref		Literature reference for the maximum [Si/H] measurement in the Hypatia Catalog.	N	47

Table 4 *continued*

Table 4 (*continued*)

Column name	Unit	Description	EMSL	Ref. #
hypatia_P_mean	dex	Mean phosphorus abundance [P/H] from the Hypatia Catalog.	N	47
hypatia_P_err [†]	dex	Phosphorus abundance uncertainty, calculated as the standard deviation of all [P/H] values from the Hypatia Catalog.	N	47
hypatia_P_nval		Number of [P/H] measurements in the Hypatia Catalog.	N	47
hypatia_P_min	dex	Minimum [P/H] in the Hypatia Catalog.	N	47
hypatia_P_minref		Literature reference for the minimum [P/H] measurement in the Hypatia Catalog.	N	47
hypatia_P_max	dex	Maximum [P/H] in the Hypatia Catalog.	N	47
hypatia_P_maxref		Literature reference for the maximum [P/H] measurement in the Hypatia Catalog.	N	47
hypatia_S_mean	dex	Mean sulfur abundance [S/H] from the Hypatia Catalog.	N	47
hypatia_S_err [†]	dex	Sulfur abundance uncertainty, calculated as the standard deviation of all [S/H] values from the Hypatia Catalog.	N	47
hypatia_S_nval		Number of [S/H] measurements in the Hypatia Catalog.	N	47
hypatia_S_min	dex	Minimum [S/H] in the Hypatia Catalog.	N	47
hypatia_S_minref		Literature reference for the minimum [S/H] measurement in the Hypatia Catalog.	N	47
hypatia_S_max	dex	Maximum [S/H] in the Hypatia Catalog.	N	47
hypatia_S_maxref		Literature reference for the maximum [S/H] measurement in the Hypatia Catalog.	N	47
hypatia_K_mean	dex	Mean potassium abundance [K/H] from the Hypatia Catalog.	N	47
hypatia_K_err [†]	dex	Potassium abundance uncertainty, calculated as the standard deviation of all [K/H] values from the Hypatia Catalog.	N	47
hypatia_K_nval		Number of [K/H] measurements in the Hypatia Catalog.	N	47
hypatia_K_min	dex	Minimum [K/H] in the Hypatia Catalog.	N	47
hypatia_K_minref		Literature reference for the minimum [K/H] measurement in the Hypatia Catalog.	N	47
hypatia_K_max	dex	Maximum [K/H] in the Hypatia Catalog.	N	47
hypatia_K_maxref		Literature reference for the maximum [K/H] measurement in the Hypatia Catalog.	N	47
hypatia_Ca_mean	dex	Mean calcium abundance [Ca/H] from the Hypatia Catalog.	N	47
hypatia_Ca_err [†]	dex	Calcium abundance uncertainty, calculated as the standard deviation of all [Ca/H] values from the Hypatia Catalog.	N	47
hypatia_Ca_nval		Number of [Ca/H] measurements in the Hypatia Catalog.	N	47
hypatia_Ca_min	dex	Minimum [Ca/H] in the Hypatia Catalog.	N	47
hypatia_Ca_minref		Literature reference for the minimum [Ca/H] measurement in the Hypatia Catalog.	N	47
hypatia_Ca_max	dex	Maximum [Ca/H] in the Hypatia Catalog.	N	47

Table 4 *continued*

Table 4 (*continued*)

Column name	Unit	Description	EMSL	Ref. #
hypatia_Ca_maxref		Literature reference for the maximum [Ca/H] measurement in the Hypatia Catalog.	N	47
hypatia_Fe_mean	dex	Mean iron abundance [Fe/H] from the Hypatia Catalog.	N	47
hypatia_Fe_err [†]	dex	Iron abundance uncertainty, calculated as the standard deviation of all [Fe/H] values from the Hypatia Catalog.	N	47
hypatia_Fe_nval		Number of [Fe/H] measurements in the Hypatia Catalog.	N	47
hypatia_Fe_min	dex	Minimum [Fe/H] in the Hypatia Catalog.	N	47
hypatia_Fe_minref		Literature reference for the minimum [Fe/H] measurement in the Hypatia Catalog.	N	47
hypatia_Fe_max	dex	Maximum [Fe/H] in the Hypatia Catalog.	N	47
hypatia_Fe_maxref		Literature reference for the maximum [Fe/H] measurement in the Hypatia Catalog.	N	47
hypatia_Ni_mean	dex	Mean nickel abundance [Ni/H] from the Hypatia Catalog.	N	47
hypatia_Ni_err [†]	dex	Nickel abundance uncertainty, calculated as the standard deviation of all [Ni/H] values from the Hypatia Catalog.	N	47
hypatia_Ni_nval		Number of [Ni/H] measurements in the Hypatia Catalog.	N	47
hypatia_Ni_min	dex	Minimum [Ni/H] in the Hypatia Catalog.	N	47
hypatia_Ni_minref		Literature reference for the minimum [Ni/H] measurement in the Hypatia Catalog.	N	47
hypatia_Ni_max	dex	Maximum [Ni/H] in the Hypatia Catalog.	N	47
hypatia_Ni_maxref		Literature reference for the maximum [Ni/H] measurement in the Hypatia Catalog.	N	47
sed_fit_npoints		Number of photometric points used to compute SED fit with ARIADNE (Vines & Jenkins 2022).	N	89
sed_model		Name of SED model favored by Bayesian model selection.	N	89
sed_model_prob		Probability of the favored SED model, derived from the Bayesian evidence.	N	89
sed_bma_teff	K	Stellar effective temperature T_{eff} derived from SED Bayesian model averaging with ARIADNE.	N	89
sed_bma_tefferr1	K	Lower T_{eff} uncertainty (1σ), derived from SED Bayesian model averaging.	N	89
sed_bma_tefferr2	K	Upper T_{eff} uncertainty (1σ), derived from SED Bayesian model averaging.	N	89
sed_bma_rad	R_{\odot}	Stellar radius R_{\star} derived from SED Bayesian model averaging with ARIADNE.	N	89
sed_bma_raderr1	R_{\odot}	Lower R_{\star} uncertainty (1σ), derived from SED Bayesian model averaging.	N	89
sed_bma_raderr2	R_{\odot}	Upper R_{\star} uncertainty (1σ), derived from SED Bayesian model averaging.	N	89
sed_grav_mass	M_{\odot}	Stellar mass M_{\star} (from $\log g$) derived from SED Bayesian model averaging with ARIADNE.	N	89
sed_grav_masserr1	M_{\odot}	Lower gravitational M_{\star} uncertainty (1σ), derived from SED Bayesian model averaging.	N	89
sed_grav_masserr2	M_{\odot}	Upper gravitational M_{\star} uncertainty (1σ), derived from SED Bayesian model averaging.	N	89

Table 4 *continued*

Table 4 (continued)

Column name	Unit	Description	EMSL	Ref. #
sed_iso_mass	M_{\odot}	Stellar mass M_{\star} (from isochrones) derived from SED Bayesian model averaging with ARIADNE.	N	89
sed_iso_masserr1	M_{\odot}	Lower isochronal M_{\star} uncertainty (1σ), derived from SED Bayesian model averaging.	N	89
sed_iso_masserr2	M_{\odot}	Upper isochronal M_{\star} uncertainty (1σ), derived from SED Bayesian model averaging.	N	89
sed_bma_lum	L_{\odot}	Stellar luminosity L_{\star} derived from SED Bayesian model averaging with ARIADNE.	N	89
sed_bma_lumerr1	L_{\odot}	Lower L_{\star} uncertainty (1σ), derived from SED Bayesian model averaging.	N	89
sed_bma_lumerr2	L_{\odot}	Upper L_{\star} uncertainty (1σ), derived from SED Bayesian model averaging.	N	89
sed_iso_age	Gyr	Stellar age (from isochrones) derived from SED Bayesian model averaging with ARIADNE.	N	89
sed_iso_ageerr1	Gyr	Lower age uncertainty (1σ), derived from SED Bayesian model averaging.	N	89
sed_iso_ageerr2	Gyr	Upper age uncertainty (1σ), derived from SED Bayesian model averaging.	N	89
tess_flare_flag		Flag indicating whether stellar flares have been detected for this target with TESS. (1=yes, 0=no).	N	89
tess_nsectors		Number of TESS sectors with two-minute cadence observations of the target.	N	89
tess_flare_count		Number of stellar flares detected during the first 39 (or 30) TESS sectors.	N	74, 97
tess_flare_rate	s^{-1}	Estimated stellar flare rate, calculated as the number of flares detected divided by the TESS observational baseline for the target.	N	89
tess_flare_Ampmax		Maximum relative flare amplitude.	N	74, 97
tess_flare_Emax	erg	Maximum estimated flare energy.	N	74, 97
tess_flare_bibcode		Reference bibcode for TESS flare rate.	N	89
Xray_flare_detection		X-ray flare detected in the XMM-Newton serendipitous source catalogue (“Y” or “N”).	N	75
tess_variability_flag		Flag indicating whether this target is variable in TESS photometry (1=yes, 0=no).	N	89
tess_variability_solution		Best model from the 19 variability analysis; can be Single-sinusoidal (1sin), Double-sinusoidal (2sin), or Auto-Correlation Function (acf).	N	27
tess_variability_sector		TESS Sector number from which this variability analysis was extracted; sp indicates the short-period periodogram search (0.01-1.5 days) was preferred.	N	27
tess_variability_period1	days	Measured photometric variability period for the first sinusoidal component.	N	27
tess_variability_period2	days	Measured photometric variability period for the second sinusoidal component.	N	27
tess_variability_period1err	days	Uncertainty in the photometric variability period for the first sinusoidal component.	N	27

Table 4 continued

Table 4 (*continued*)

Column name	Unit	Description	EMSL	Ref. #
tess_variability_period2err	days	Uncertainty in the photometric variability period for the second sinusoidal component.	N	27
tess_variability_amp1	ppm	Flux amplitude of photometric variability for the first sinusoidal component.	N	27
tess_variability_amp2	ppm	Flux amplitude of photometric variability for the second sinusoidal component.	N	27
tess_variability_amp1err	ppm	Uncertainty in the flux amplitude of photometric variability for the first sinusoidal component.	N	27
tess_variability_amp2err	ppm	Uncertainty in the flux amplitude of photometric variability for the second sinusoidal component.	N	27
aavso_variable_flag		Flag indicating whether this target is included in the AAVSO VSX Catalog (1=yes, 0=no).	N	89
aavso_variable_name		Source name in the AAVSO VSX Catalog.	N	89
aavso_variable_status		Source variability status in the AAVSO VSX Catalog (“V”=variable, “S”=suspected variable).	N	89
aavso_variable_link		URL link to the VSX entry for this source.	N	89
Xray_flag		Flag indicating whether this target has a previous X-ray detection (1=yes, 0=no).	N	89
morx_name		Object ID from the literature adopted in the MORX Catalog.	N	28, 29
morx_Xraypct		The calculated percent likelihood that the shown X-ray detection(s) is associated with this optical object.	N	28, 29
morx_starpct		The calculated percentage likelihood that the X-ray associated object is a star.	N	28, 29
morx_chandra_id		Chandra X-ray detection ID, if any.	N	28, 29
morx_xmm_id		XMM-Newton X-ray detection ID, if any.	N	28, 29
morx_swift_id		SWIFT X-ray detection ID, if any.	N	28, 29
morx_other_id		ROSAT or XMM-Slew X-ray detection ID, if any.	N	28, 29

Table 4 *continued*

Table 4 (continued)

Column name	Unit	Description	EMSL	Ref. #
-------------	------	-------------	------	--------

*Mamajek & Stapelfeldt (2023) either adopted Cousins R_c magnitudes from the literature or estimated them based on Gaia EDR3 G and G_{RP} photometry or by adopting an intrinsic $V - R_c$ color for the star's spectral type.

† If only a single abundance measurement was identified in the catalog, we provide an estimate of the uncertainty as the median [Fe/H] uncertainty from the entire sample (0.065 dex).

References—¹Abt (1981); ²Abt (2009); ³Akeson et al. (2021); ⁴Anders et al. (2019); ⁵Baliunas et al. (1996); ⁶Bessel (1990); ⁷Bianchi et al. (2017); ⁸Boro Saikia et al. (2018); ⁹Boyajian et al. (2012); ¹⁰Boyajian et al. (2013); ¹¹Brown et al. (2022); ¹²Cannon & Pickering (1993); ¹³Casagrande et al. (2011); ¹⁴Corbally (1984); ¹⁵Cousins (1980); ¹⁶Cowley et al. (1967); ¹⁷Cowley (1976); ¹⁸Cutri et al. (2003); ¹⁹Cutri et al. (2021); ²⁰David & Hillenbrand (2015); ²¹Dieterich et al. (2012); ²²Duncan et al. (1991); ²³Eggen (1965); ²⁴Eggenberger et al. (2008); ²⁵ESA (1997a); ²⁶ESA (1997b); ²⁷Fetherolf et al. (2023); ²⁸Flesch (2016); ²⁹Flesch (2023); ³⁰Fuhrmann (2008); ³¹Gaia Collaboration et al. (2018); ³²Gaia Collaboration (2022a); ³³Gaia Collaboration (2022b); ³⁴Gaia Collaboration et al. (2023); ³⁵Gáspár et al. (2016); ³⁶Gliese & Jahreiß (1991); ³⁷Golovin et al. (2023); ³⁸Gomes da Silva et al. (2021); ³⁹Gondoin (2020); ⁴⁰Gray (1989); ⁴¹Gray et al. (2001); ⁴²Gray et al. (2003); ⁴³Gray et al. (2006); ⁴⁴Hall et al. (2007); ⁴⁵Hauck & Mermilliod (1998); ⁴⁶Henry et al. (1996); ⁴⁷Hinkel & Unterborn (2018); ⁴⁸Hoffleit & Jaschek (1991); ⁴⁹Høg et al. (2000); ⁵⁰Houk & Cowley (1975); ⁵¹Huang et al. (2015); ⁵²Isaacson & Fischer (2010); ⁵³Keenan & McNeil (1989); ⁵⁴Kervella et al. (2017); ⁵⁵Kharchenko (2001); ⁵⁶King et al. (2003); ⁵⁷Kirkpatrick et al. (1991); ⁵⁸Lee (1984); ⁵⁹Lindgren & Heiter (2017); ⁶⁰Luck & Heiter (2005); ⁶¹Maldonado et al. (2010); ⁶²Mamajek & Stapelfeldt (2023); ⁶³Mason et al. (2001); ⁶⁴Mermilliod (1997); ⁶⁵Mermilliod et al. (1997); ⁶⁶Meunier et al. (2022); ⁶⁷Montes et al. (2018); ⁶⁸Morgan & Keenan (1973); ⁶⁹Murgas et al. (2013); ⁷⁰Newton et al. (2015); ⁷¹Pace (2013); ⁷²Paunzen (2015); ⁷³Pickles & Depagne (2010); ⁷⁴Pietras et al. (2022); ⁷⁵Pye et al. (2015); ⁷⁶Radick et al. (2018); ⁷⁷Ramírez et al. (2013); ⁷⁸Rocha-Pinto et al. (2004); ⁷⁹Saffe et al. (2005); ⁸⁰Samus et al. (2017); ⁸¹Schröder et al. (2009); ⁸²Schweitzer et al. (2019); ⁸³Soubiran et al. (2022); ⁸⁴Stanford-Moore et al. (2020); ⁸⁵Stassun et al. (2018); ⁸⁶Stassun et al. (2019); ⁸⁷Takeda et al. (2005); ⁸⁸Takeda et al. (2007); ⁸⁹This work; ⁹⁰Torres et al. (2006); ⁹¹Twarog & Anthony-Twarog (1995); ⁹²Valenti & Fischer (2005); ⁹³van Leeuwen (2007); ⁹⁴Vican (2012); ⁹⁵Woolf & Wallerstein (2005); ⁹⁶Wright et al. (2004); ⁹⁷Yang et al. (2023); ⁹⁸Yee et al. (2017); ⁹⁹Zorec & Royer (2012)